ORBITAL ADVECTION BY INTERPOLATION: A FAST AND ACCURATE NUMERICAL SCHEME FOR SUPER-FAST MHD FLOWS

Bryan M. Johnson[*], Xiaoyue Guan and Charles F. Gammie
Center for Theoretical Astrophysics, University of Illinois at Urbana-Champaign, 1110 West Green St., Urbana, IL 61801
Draft version July 21, 2008

ABSTRACT

In numerical models of thin astrophysical disks that use an Eulerian scheme, gas orbits supersonically through a fixed grid. As a result the time step is sharply limited by the Courant condition. Also, because the mean flow speed with respect to the grid varies with position, the truncation error varies systematically with position. For hydrodynamic (unmagnetized) disks an algorithm called FARGO has been developed that advects the gas along its mean orbit using a separate interpolation substep. This relaxes the constraint imposed by the Courant condition, which now depends only on the peculiar velocity of the gas, and results in a truncation error that is more nearly independent of position. This paper describes a FARGO-like algorithm suitable for evolving magnetized disks. Our method is second order accurate on a smooth flow and preserves $\boldsymbol{\nabla} \cdot \boldsymbol{B} = 0$ to machine precision. The main restriction is that $\boldsymbol{B}$ must be discretized on a staggered mesh. We give a detailed description of an implementation of the code and demonstrate that it produces the expected results on linear and nonlinear problems. We also point out how the scheme might be generalized to make the integration of other supersonic/super-fast flows more efficient. Although our scheme reduces the variation of truncation error with position, it does not eliminate it. We show that the residual position dependence leads to characteristic radial variations in the density over long integrations.

Subject headings: numerical methods, magnetohydrodynamics

1. INTRODUCTION

Numerical experiments have played a key role in advancing our understanding of accretion disk dynamics. Future attacks on the main unsolved problems of disk theory, such as the evolution of large-scale magnetic fields in disks, will also likely benefit from numerical experiments. But numerical work is always limited by current hardware and algorithms. Here we describe a new algorithm for evolving the magnetohydrodynamic (MHD) equations that is designed to speed up, and improve the quality of, future disk experiments.

The majority of numerical hydrodynamic studies of disks use an *Eulerian* approach: the fluid equations are discretized in a fixed frame and the code "pushes" the fluid through the grid. In an accretion disk the fluid velocity can be written

$$\boldsymbol{v} = \boldsymbol{v}_{orb} + \Delta \boldsymbol{v} \qquad (1)$$

where $\boldsymbol{v}_{orb}$ is the circular orbit velocity, and $\Delta \boldsymbol{v}$ represents departures from a circular orbit caused by, e.g., turbulence. If the equations are discretized in a nonrotating frame then typically an Eulerian scheme will have to push fluid through the grid with a speed that varies systematically with radius r. As a result the truncation error will vary with position, possibly yielding misleading results.

Another disadvantage of a straightforward Eulerian approach has to do with the Courant condition on the time step Δt:

$$\Delta t < \frac{C}{V \Delta L} \qquad (2)$$

where $C \sim 1$ is the Courant number, V is the fastest wave speed in the problem, and ΔL is the grid scale. If one

is interested in a cold accretion disk with $|\Delta \boldsymbol{v}| \sim c_s \ll |\boldsymbol{v}_{orb}|$ ($c_s \equiv$ sound speed), then V will be dominated by the orbital motion, i.e. $V \approx r\Omega$. This implies small time steps: the code is only allowed to push the fluid along its orbit by a fraction of a zone per time step. Most of the computational time will be spent on orbital advection.

All this runs contrary to one's sense that somehow the peculiar motion $\Delta \boldsymbol{v}$ should control the time step and the truncation error. After all, in a frame moving on a circular orbit one expects that the motion of the fluid is either subsonic or near-sonic.

Three strategies have been employed to get around these two issues. First, one can work in a rotating frame. This works well only within a few scale heights $H \equiv c_s/\Omega$ of the corotation radius. Second, one can employ a Lagrangian scheme, which follows individual fluid elements. In astrophysical applications this usually means smoothed particle hydrodynamics (SPH). SPH has intrinsic noise that makes it unsuitable for many sensitive disk dynamics problems. It is also difficult, in our experience, to incorporate magnetic fields into SPH. Third, one can adopt a hybrid, quasi-Lagrangian scheme that treats the orbital advection separately. This is the approach advanced by Masset (2000) in his FARGO code, and later by Gammie (2001), Johnson & Gammie (2003) and Johnson & Gammie (2005). Our contribution here is to extend this method to MHD.

There are two other possible strategies that we are aware of for addressing these problems in the context of disks. First, one can do an orbitally-centered domain decomposition in a parallelized code (Caunt & Korpi 2001). Each processor works on a small portion of the grid ($\lesssim H$) without orbital advection, and then orbital advection is used in the boundary conditions to link the small portions together. Second, one could employ a

*Current address: Lawrence Livermore National Laboratory, L-413, 7000 East Avenue, Livermore, CA 94550-9698

fully Lagrangian orbital advection by defining the grid in shearing coordinates, coupled to a remap (similar to what is done here) once per shear time $(q\Omega)^{-1}$ (Narayan, private communication) at the risk of introducing a new, numerical timescale into the problem. This is what is done in some spectral schemes for incompressible shear flows (e.g., Umurhan & Regev 2004).

The main idea in the approach we take here is to operator-split the update of the fluid variables. The evolution equation for each dependent fluid variable F is

$$\frac{\partial F}{\partial t} = -(\boldsymbol{v} \cdot \boldsymbol{\nabla})F + \mathcal{L}, \tag{3}$$

where the first term on the rhs is advection (its form is determined by Galilean invariance), and the second term $\mathcal{L}$ contains everything else. The advection operator can, in turn, be split again:

$$\frac{\partial F}{\partial t} = -(\boldsymbol{v}_{orb} \cdot \boldsymbol{\nabla})F - (\Delta\boldsymbol{v} \cdot \boldsymbol{\nabla})F + \mathcal{L}, \tag{4}$$

The orbital advection operator simply pushes the fluid elements along its orbit. Remarkably, this can be done using an interpolation formula that is not constrained by the Courant condition! One simply needs to know

$$\boldsymbol{x}(t) = \int^t dt' \, \boldsymbol{v}_{orb}(t') \tag{5}$$

in advance, so that the fluid variable $F(\boldsymbol{x}[t + \Delta t])$ can be interpolated from known values near $F(\boldsymbol{x}[t])$. The method can be made formally second-order accurate using Strang splitting. Notice that this idea can be applied to *any* flow with known orbits, not just circular, Keplerian orbits for disks.

Implementing a stable, accurate orbital advection operator involves a surprising amount of bookkeeping, particularly when one must maintain a divergence-free magnetic field. In this paper we describe an implementation for a particular context, albeit one of considerable interest: the "local model" for astrophysical disks. The plan of the paper is as follows. In §2 we write down the basic equations describing our model, and show how the advection can be split into pieces corresponding to the orbital and peculiar velocities. In §3 we summarize our algorithm, deferring its rather tedious derivation to Appendix A. In §4 we describe tests of the method. §5 describes a sample nonlinear application. We have incorporated our algorithm into a ZEUS-like code for performing calculations. §6 summarizes the results and identifies the key formulae for implementing our scheme.

2. BASIC EQUATIONS

The "local model" for astrophysical disks is obtained by expanding the equations of motion around a circular-orbiting coordinate origin at cylindrical coordinates $(r, \phi, z) = (r_o, \Omega_o t + \phi_o, 0)$, assuming that the peculiar velocities are comparable to the sound speed and that the sound speed is small compared to the orbital speed. The local Cartesian coordinates are obtained from cylindrical coordinates via $(x, y, z) = (r - r_o, r_o[\phi - \Omega_o t - \phi_o], z)$.

In this context the equations of isothermal ideal MHD consist of seven evolution equations, given by

$$\frac{\partial \rho}{\partial t} + \boldsymbol{\nabla} \cdot (\rho\boldsymbol{v}) = 0, \tag{6}$$

$$\frac{\partial \boldsymbol{v}}{\partial t} + \boldsymbol{v}\cdot\boldsymbol{\nabla}\boldsymbol{v} + c_s^2\frac{\boldsymbol{\nabla}\rho}{\rho} + \frac{\boldsymbol{\nabla}B^2}{8\pi\rho} - \frac{(\boldsymbol{B}\cdot\boldsymbol{\nabla})\boldsymbol{B}}{4\pi\rho} + 2\boldsymbol{\Omega}\times\boldsymbol{v} - 2q\Omega^2 x\,\hat{\boldsymbol{x}} = 0, \tag{7}$$

$$\frac{\partial \boldsymbol{B}}{\partial t} - \boldsymbol{\nabla} \times (\boldsymbol{v} \times \boldsymbol{B}) = 0, \tag{8}$$

plus the divergence-free constraint on the magnetic field:

$$\boldsymbol{\nabla} \cdot \boldsymbol{B} = 0. \tag{9}$$

The final two terms in equation (7) represent the Coriolis and tidal forces in the local frame. The orbital velocity is

$$\boldsymbol{v}_{orb} = -q\Omega x\,\hat{\boldsymbol{y}}, \tag{10}$$

where

$$q \equiv -\frac{1}{2}\frac{d\ln\Omega^2}{d\ln r} \tag{11}$$

is the shear parameter. One can readily verify that this velocity, along with a constant density and zero magnetic field, is a steady-state solution to equation (7).

Integrating equation (9) over a control volume and expressing the volume integral as a surface integral via Gauss's Law gives an alternative representation of the divergence-free constraint:

$$\Phi \equiv \int_A \boldsymbol{B} \cdot \hat{\boldsymbol{n}}\, da = 0, \tag{12}$$

where A is the surface bounding the volume, da is an area element in that surface and $\hat{\boldsymbol{n}}$ is a unit vector normal to the surface. Satisfying expression (12) throughout the evolution of equations (6)-(8) is one of the main challenges in numerical MHD.

The evolution equations (6)-(8) can be recast using $\boldsymbol{v} = \boldsymbol{v}_{orb} + \Delta\boldsymbol{v}$:

$$\frac{\partial\rho}{\partial t} + \boldsymbol{v}_{orb} \cdot \boldsymbol{\nabla}\rho + \boldsymbol{\nabla} \cdot (\rho\,\Delta\boldsymbol{v}) = 0, \tag{13}$$

$$\frac{\partial\Delta\boldsymbol{v}}{\partial t} + \boldsymbol{v}_{orb} \cdot \boldsymbol{\nabla}(\Delta\boldsymbol{v}) + \Delta\boldsymbol{v} \cdot \boldsymbol{\nabla}(\Delta\boldsymbol{v}) + c_s^2\frac{\boldsymbol{\nabla}\rho}{\rho}$$
$$+ \frac{\boldsymbol{\nabla}B^2}{8\pi\rho} - \frac{\boldsymbol{B}\cdot\boldsymbol{\nabla}\boldsymbol{B}}{4\pi\rho} + 2\boldsymbol{\Omega} \times \Delta\boldsymbol{v} - q\Omega\,(\Delta v)_x\,\hat{\boldsymbol{y}} = 0, \tag{14}$$

$$\frac{\partial\boldsymbol{B}}{\partial t} + \boldsymbol{v}_{orb} \cdot \boldsymbol{\nabla}\boldsymbol{B} - \boldsymbol{\nabla} \times (\Delta\boldsymbol{v} \times \boldsymbol{B}) + q\Omega B_x\,\hat{\boldsymbol{y}} = 0, \tag{15}$$

There are three differences between equations (13)-(15) and the original equations (6)-(8): 1) each equation has an additional transport term due to the orbital (mean shear) velocity, $\boldsymbol{v}_{orb} \cdot \boldsymbol{\nabla}$, 2) the tidal term in equation (7) has been replaced by $-q\Omega\,(\Delta v)_x\,\hat{\boldsymbol{y}}$ in equation (14) and 3) there is an additional term $q\Omega B_x\hat{\boldsymbol{y}}$ in equation (15). The latter two terms reflect the conversion of radial velocity and magnetic field components into azimuthal components by the shear. The last term in equation (14) can simply be treated as an additional term in the finite-difference algorithm, whereas the last term in equation (15) must be treated differently, using the algorithm we outline in this paper, in order to preserve the divergence-free constraint.

The local model is usually simulated using the "shearing box" boundary conditions (e.g. Hawley et al. 1995). These boundary conditions isolate a rectangular region in the disk. The azimuthal (y) boundary conditions are

periodic; the radial (x) boundary conditions are "nearly periodic", i.e. they connect the radial boundaries in a time-dependent way that enforces the mean shear flow; and one is free to choose the vertical boundary conditions for physical and numerical convenience.

3. ALGORITHM

The orbital advection substep consists of evaluating the fluid variable F at time $t + \Delta t$ using interpolation:

$$F(x, y, z, t + \Delta t) = F(x, y + q\Omega x \Delta t, z, t). \quad (16)$$

Methods for stable interpolation of the independent variables are well known. An implementation for hydrodynamical variables is described for the local model by Gammie (2001).

The interpolation can be thought of as shifting a single column of zones (at constant x and z) by what is generally a noninteger number of zones. The shift can then be decomposed into an integer number of zones and a fractional shift of up to half a zone. The integral shift can be done trivially, while the fractional zone shift is best done using the same transport algorithm as the rest of the code.

The induction equation must be treated differently because of the $\boldsymbol{\nabla} \cdot \boldsymbol{B} = 0$ constraint. In our code the magnetic field is discretized on a staggered mesh, and magnetic field variables represent fluxes through zone faces. The effect of orbital advection on the zone faces in the $x - y$ plane is illustrated in Figure 1. The dashed lines show the positions of the "old" zone faces after they have been sheared through a time Δt. The solid lines show the "new" zone faces onto which the fluxes from the old zone faces must be interpolated. Flux freezing requires that the fluxes through the old zone faces be preserved by the orbital advection; our algorithm simply interpolates the fluxes in these sheared zones onto the new zones in a way that preserves $\boldsymbol{\nabla} \cdot \boldsymbol{B} = 0$.

3.1. Definitions

The shear has two effects on each zone of the old grid: 1) a linear distortion of the zone in the azimuthal direction, and 2) an azimuthal advection of the zone that depends upon the radial position of the zone in the old grid. We quantify these two effects with the following definitions:

$$s \equiv \frac{q\Omega\Delta x\Delta t}{\Delta y} \quad (17)$$

is the relative shift (in dimensionless zone units) of a fluid element across a single zone in one time step ($-s\Delta y/\Delta x$ is the slope of the diagonal lines in Figure 1), and

$$S \equiv \frac{v_{orb}\,\Delta t}{\Delta y} = \frac{-q\Omega x\,\Delta t}{\Delta y} \quad (18)$$

is the amount (in dimensionless zone units) that a fluid element is advected by the shear in one time step. In general, S is composed of a non-integral number of zones, which we divide into an integral part $\mathrm{NINT}(S)$ and a fractional part

$$f \equiv S - \mathrm{NINT}(S). \quad (19)$$

Here $\mathrm{NINT}(S)$ is the value of S rounded to the nearest integer, so that f can take on both positive and negative values.

We denote old zones by the superscript n and new zones by the superscript $n + 1$. The indices i, j, k correspond to the x, y, z directions. The azimuthal index for an old zone goes from j to

$$J \equiv j - \mathrm{NINT}(S) \quad (20)$$

after each time step Δt.

3.2. Interpolation Formulae

We can obtain divergence-free interpolation formulae by considering a control volume (which we will call a *subvolume*, because it is smaller than a zone) bounded by portions of zone faces from both the old grid and the new grid (which we will call *subfaces*, because they are in general smaller than a full zone face), and requiring that the sum of the fluxes into or out of that volume is zero.

There are three distinct cases that occur when mapping the old, sheared grid onto the new grid, depending on whether f is positive or negative and whether or not the azimuthal face of a sheared grid zone intersects the azimuthal face of a new grid zone. The three cases are illustrated in Figures 2-4, and correspond to $|f|/s < 1/2$ (Case 1), $f/s > 1/2$ (Case 2) and $f/s < -1/2$ (Case 3). The value of f/s depends, in turn, on the x coordinate of the zone and the time step (see Figure 1).

Deducing the fluxes through the faces of the new zones is a matter of frankly tedious bookkeeping that is described in detail in Appendix A but summarized here. First, in each case write the constraint that the sum of the fluxes in and out of each subvolume vanish ($\boldsymbol{\nabla} \cdot \boldsymbol{B} = 0$). Next, solve for the unknown fluxes through the subfaces of the new grid in terms of the fluxes through the subfaces of the old grid. The latter can be deduced given a model for the variation of the field strength over each zone face in the old grid; we use a linear model with van Leer slopes, consistent with the rest of our ZEUS-like code. Finally, sum the fluxes through the subfaces to obtain the flux through each face of the new grid.

The final formulae are given below, where the w coefficients appearing in these expressions are defined in Table A1 and the dq's are van Leer slopes:

Radial field update, Case 1:

$$\begin{aligned} bx_{ijk}^{n+1} = bx_{iJk}^n &+ w_{10}(bx_{iJ-1k}^n - bx_{iJk}^n) \\ &+ w_{11}(bx\_dqy_{iJ-1k}^n - bx\_dqy_{iJk}^n), \quad (21) \end{aligned}$$

Radial field update, Case 2:

$$\begin{aligned} bx_{ijk}^{n+1} = bx_{iJk}^n &+ w_{20}(bx_{iJ-1k}^n - bx_{iJk}^n) \\ &+ w_{21}(bx\_dqy_{iJ-1k}^n - bx\_dqy_{iJk}^n), \quad (22) \end{aligned}$$

Radial field update, Case 3:

$$\begin{aligned} bx_{ijk}^{n+1} = bx_{iJk}^n &+ w_{30}(bx_{iJ+1k}^n - bx_{iJk}^n) \\ &+ w_{31}(bx\_dqy_{iJ+1k}^n - bx\_dqy_{iJk}^n). \quad (23) \end{aligned}$$

Azimuthal field update, Case 1, n even:

$$by_{ijk}^{n+1} = \frac{1}{2}\left[by_{iJk}^n + by_{iJ+1k}^n + \frac{\Delta y}{\Delta x}\left(bx_{i+1Jk}^n - bx_{iJk}^n\right)\right.$$

$$+ \frac{\Delta y}{\Delta z}\left(bz_{iJk+1}^n - bz_{iJk}^n\right)\Big] + \frac{\Delta y}{\Delta x}\Big[-w_{10}bx_{iJ-1k}^n$$

$$- w_{12}bx_{i+1Jk}^n - w_{11}bx\_dqy_{iJ-1k}^n - w_{13}bx\_dqy_{i+1Jk}^n\Big]$$

$$+ \frac{\Delta y}{\Delta z}\left[w_{14}(bz_{iJ-1k+1}^n - bz_{iJ-1k}^n) + w_{17}(bz_{iJk}^n - bz_{iJk+1}^n)\right.$$

$$+ w_{15}(bz\_dqx_{iJ-1k+1}^n - bz\_dqx_{iJ-1k}^n) + w_{16}(bz\_dqy_{iJ-1k+1}^n$$

$$- bz\_dqy_{iJ-1k}^n) + w_{18}(bz\_dqx_{iJk}^n - bz\_dqx_{iJk+1}^n)$$

$$\left. + w_{19}(bz\_dqy_{iJk}^n - bz\_dqy_{iJk+1}^n)\right]. \quad (24)$$

Azimuthal field update, Case 1, n odd:

$$by_{ijk}^{n+1} = \frac{1}{2}\left[by_{iJk}^n + by_{iJ-1k}^n + \frac{\Delta y}{\Delta x}\left(bx_{iJ-1k}^n - bx_{i+1J-1k}^n\right)\right.$$

$$+ \frac{\Delta y}{\Delta z}\left(bz_{iJ-1k}^n - bz_{iJ-1k+1}^n\right)\Big] + \frac{\Delta y}{\Delta x}\Big[-w_{10}bx_{iJ-1k}^n$$

$$- w_{12}bx_{i+1Jk}^n - w_{11}bx\_dqy_{iJ-1k}^n - w_{13}bx\_dqy_{i+1Jk}^n\Big]$$

$$+ \frac{\Delta y}{\Delta z}\left[w_{14}(bz_{iJ-1k+1}^n - bz_{iJ-1k}^n) + w_{15}(bz\_dqx_{iJ-1k+1}^n\right.$$

$$- bz\_dqx_{iJ-1k}^n) + w_{16}(bz\_dqy_{iJ-1k+1}^n - bz\_dqy_{iJ-1k}^n)$$

$$+ w_{17}(bz_{iJk}^n - bz_{iJk+1}^n) + w_{18}(bz\_dqx_{iJk}^n - bz\_dqx_{iJk+1}^n)$$

$$\left. + w_{19}(bz\_dqy_{iJk}^n - bz\_dqy_{iJk+1}^n)\right]. \quad (25)$$

Azimuthal field update, Case 2:

$$by_{ijk}^{n+1} = \frac{1}{2}\left[by_{iJk}^n + by_{iJ-1k}^n + \frac{\Delta y}{\Delta x}\left(bx_{iJ-1k}^n - bx_{i+1J-1k}^n\right)\right.$$

$$+ \frac{\Delta y}{\Delta z}\left(bz_{iJ-1k}^n - bz_{iJ-1k+1}^n\right)\Big] + \frac{\Delta y}{\Delta x}\Big[-w_{20}bx_{iJ-1k}^n$$

$$+ w_{22}bx_{i+1J-1k}^n - w_{21}bx\_dqy_{iJ-1k}^n + w_{23}bx\_dqy_{i+1J-1k}^n\Big]$$

$$+ \frac{\Delta y}{\Delta z}\left[w_{24}(bz_{iJ-1k+1}^n - bz_{iJ-1k}^n) + w_{25}(bz\_dqx_{iJ-1k+1}^n\right.$$

$$\left. - bz\_dqx_{iJ-1k}^n) + w_{26}(bz\_dqy_{iJ-1k+1}^n - bz\_dqy_{iJ-1k}^n)\right]. \quad (26)$$

Azimuthal field update, Case 3:

$$by_{ijk}^{n+1} = \frac{1}{2}\left[by_{iJk}^n + by_{iJ+1k}^n + \frac{\Delta y}{\Delta x}\left(bx_{i+1Jk}^n - bx_{iJk}^n\right)\right.$$

$$+ \frac{\Delta y}{\Delta z}\left(bz_{iJk+1}^n - bz_{iJk}^n\right)\Big]\frac{\Delta y}{\Delta x}\Big[w_{30}bx_{iJk}^n - w_{32}bx_{i+1Jk}^n$$

$$+ w_{31}bx\_dqy_{iJk}^n - w_{33}bx\_dqy_{i+1Jk}^n\Big]\frac{\Delta y}{\Delta z}\Big[w_{34}(bz_{iJk}^n$$

$$- bz_{iJk+1}^n)w_{35}(bz\_dqx_{iJk}^n - bz\_dqx_{iJk+1}^n)$$

$$\left. + w_{36}(bz\_dqy_{iJk}^n - bz\_dqy_{iJk+1}^n)\right]. \quad (27)$$

Vertical field update, Case 1:

$$bz_{ijk}^{n+1} = bz_{iJk}^n + w_{14}(bz_{iJ-1k}^n - bz_{iJk}^n) + w_{17}(bz_{iJ+1k}^n - bz_{iJk}^n)$$

$$+ w_{15}(bz\_dqx_{iJ-1k}^n - bz\_dqx_{iJk}^n) + w_{16}(bz\_dqy_{iJ-1k}^n$$

$$- bz\_dqy_{iJk}^n) + w_{18}(bz\_dqx_{iJ+1k}^n - bz\_dqx_{iJk}^n)$$

$$+ w_{19}(bz\_dqy_{iJ+1k}^n - bz\_dqy_{iJk}^n), \quad (28)$$

Vertical field update, Case 2:

$$bz_{ijk}^{n+1} = bz_{iJk}^n + w_{24}(bz_{iJ-1k}^n - bz_{iJk}^n)$$

$$+ w_{25}(bz\_dqx_{iJ-1k}^n - bz\_dqx_{iJk}^n)$$

$$+ w_{26}(bz\_dqy_{iJ-1k}^n - bz\_dqy_{iJk}^n), \quad (29)$$

Vertical field update, Case 3:

$$bz_{ijk}^{n+1} = bz_{iJk}^n + w_{34}(bz_{iJ+1k}^n - bz_{iJk}^n)$$

$$+ w_{35}(bz\_dqx_{iJ+1k}^n - bz\_dqx_{iJk}^n)$$

$$+ w_{36}(bz\_dqy_{iJ+1k}^n - bz\_dqy_{iJk}^n). \quad (30)$$

4. TESTS

We have tested our algorithm on both linear and nonlinear problems. Linear perturbations in the local model are decomposed most naturally in terms of shearing waves, or shwaves, which appear spatially as plane waves in a frame comoving with the shear. The radial wavenumber of a shwave increases linearly with time and its amplitude does not in general have an exponential time dependence (as does a normal mode). Details on shwaves in isothermal MHD are given in Johnson (2007) and summarized in Appendix B. We have calculated the evolution of both compressive and incompressive shwaves as a function of numerical resolution, and the results are shown in Figures 5-11.

We employ a grid of physical size $L_x \times L_y \times L_z$ and numerical resolution $N_x \times N_y \times N_z$. The equilibrium state about which we perturb has a constant density ρ_0 and spatially constant magnetic field $\boldsymbol{B}_0$, plus the background shear flow. On this background state we impose a plane wave perturbation with initial amplitude $(\delta\rho, \delta\boldsymbol{v}, \delta\boldsymbol{B})$ and initial wavevector $\boldsymbol{k} = 2\pi(m_x/L_x, m_y/L_y, m_z/L_z)$, where $m_x/m_y < 0$ corresponds to a shwave that initially leads the mean shear. The perturbations are expressed in units with $\rho_0 = c_s = 1$.

Our first linear test is a simple advection of the magnetic field components with zero velocity perturbation, for a shwave that swings from leading to trailing. Different operators in an operator split scheme do not necessarily converge at the same rate; the overall convergence rate depends upon the combined convergence properties of each operation. This test is therefore important for isolating the convergence properties of our algorithm. For this test, we employ equal box dimensions $L = 4H$ and equal numerical resolutions N. The other parameters for this run are $m_x = -1$, $m_y = m_z = 1$, and $B_0 = 0$. The initial perturbation is $\delta\rho = \delta\boldsymbol{v} = 0$ and $\delta\boldsymbol{B} = 10^{-6}(2, 1, 1)\cos(\boldsymbol{k} \cdot \boldsymbol{l})$, where $\boldsymbol{l} \equiv (x, y, z)$. The amplitude of these shwaves is constant with time. Figure 5 shows the evolution of the vertical field component at $N = 8, 16, 32$ and 64.

The convergence properties of our algorithm for this test are shown in Figure 6, which is a plot of the L1

norm of the error in each magnetic field component as a function of numerical resolution N. Also shown on this plot are the convergence properties of a run with orbital advection turned off, for comparison purposes. The algorithm converges at second order, as expected.

To demonstrate the improved accuracy obtained by using orbital advection, we have run the same test at various box sizes. Figure 7 shows the L1 norm of the error in the azimuthal field component in runs with $L = H$ and $L = 10H$, both with and without orbital advection. The errors are comparable in the run with $L = H$, but in the run with $L = 10H$ the errors with orbital advection are smaller by a factor of ~ 4. For our second-order algorithm, this corresponds to a gain in effective resolution (at fixed error) of ~ 2 (for $L = 10H$). Orbital advection is more efficient in addition to being more accurate, particularly when the box size is large compared to H. For example, at $N = 64$, the ratio of zone cycles with orbital advection on and off is ~ 0.8 in runs with $L = H$; this ratio decreases to ~ 0.2 in runs with $L = 10H$.

Figure 8 shows the evolution of the radial field perturbation for an incompressive shwave that grows nearly exponentially as it swings from leading to trailing. The parameters for this run are $L_x = L_y = 10H$, $L_z = H$, $m_x = -2$, $m_y = m_z = 1$, $N_y = N_z = N_x/2$, and $\boldsymbol{B}_0 = \sqrt{15/16}(\Omega/k_z)\hat{\boldsymbol{z}}$.[1] The initial perturbation is $\delta\rho = 8.95250 \times 10^{-10} \cos(\boldsymbol{k} \cdot \boldsymbol{l} - \pi/4)$, $\delta\boldsymbol{v} = 10^{-8}(8.16589, 8.70641, 0.762537) \cos(\boldsymbol{k} \cdot \boldsymbol{l} + \pi/4)$, and $\delta\boldsymbol{B} = 10^{-7}(-1.08076, 1.04172, -0.320324) \cos(\boldsymbol{k} \cdot \boldsymbol{l} - \pi/4)$.

As discussed by Johnson & Gammie (2005), aliasing of incompressive shwaves can artificially convert trailing shwaves into leading shwaves. Figure 9 shows the long term evolution of the previous run, demonstrating that aliasing can result in artificial growth in the linear regime. We do not consider this to be a serious problem for a nonlinear calculation, however, such as the development of turbulence due to the MRI. The growth rate due to aliasing cannot exceed the MRI growth rate in the linear regime, and the evolution in the nonlinear regime is dominated by small scale fluctuations that interact on a time scale much shorter than the shear time scale. In addition, the strong aliasing seen in Figure 9 depends upon the very small amount of diffusion present in this test due to the lack of any motion with respect to the grid. To introduce numerical diffusion, we perform the same test with an additional bulk epicyclic motion of the grid superimposed (amplitude $\sim 0.1c_s$). As shown in Figure 10, a small amount of diffusion can significantly reduce the effects of aliasing.

Figure 11 shows the evolution of the azimuthal field perturbation for a compressive shwave. The parameters for this run are $L = 0.5H$, $m_x = -2$, $m_y = m_z = 1$, $N_y = N_z = N_x/2$, and $\boldsymbol{B}_0 = (0.1, 0.2, 0.0)$. The initial perturbation is $\delta\rho = 5.48082 \times 10^{-6} \cos(\boldsymbol{k} \cdot \boldsymbol{l})$, $\delta\boldsymbol{v} = 2.29279 \times 10^{-6}(-2.0, 1.0, 1.0) \cos(\boldsymbol{k} \cdot \boldsymbol{l})$, and $\delta\boldsymbol{B} = \boldsymbol{B}_0\delta\rho$. The frequency of these shwaves increases as t^2 at late times, due to the linear increase with time of both the radial wavenumber and v_A in the presence of a radial field. Our algorithm clearly produces convergent results on this problem as well.

5. SAMPLE NONLINEAR CALCULATION

The purpose of developing this algorithm is to enable new, large shearing box models of disks. Here we describe one fruit of this labor: a sample shearing box calculation that illustrates the capability of the code. Our model has size $L_x \times L_y \times L_z = 8H \times 8\pi H \times 2H$.[2] It is unstratified, with periodic boundary conditions in the vertical direction. The resolution is $N_x \times N_y \times N_z = 128 \times 128 \times 64$. The model starts with $B_z = (\sqrt{15}/[32\pi]) \sin(\pi x)$, so the model has zero net vertical field. Velocity perturbations of amplitude $0.01c_s$ are added to each zone.

Figure 12 shows the evolution of α. As expected, the magnetorotational instability grows sharply after a few rotation periods. The flow then reaches a nonlinear regime, followed by saturation. The model saturates at $\alpha \approx 0.01$, broadly consistent with the earlier work of Hawley et al. (1995) and others.

The upper panel of Figure 13 shows a snapshot of density on a two dimensional slice at $z = 0$ at the end of the run $t = 100\Omega^{-1}$. Notice the trailing spiral structures, which have an azimuthal extent comparable to the size of the box. Also notice that the radial extent of these structures is of order H, indicating that, at least in the context of this simulation, the correlation function for the turbulence is of limited radial extent. We will explore this idea further in a later publication.

For comparison, we have run the same problem with the original ZEUS[3] (Stone & Norman 1992a,b). In the lower panel of Figure 13 we plot a $z = 0$ density slice at $t = 100\Omega^{-1}$ for the original ZEUS run. Figure 14 shows the evolution of the volume averaged magnetic energy density for both runs; the run with orbital advection is shown as a solid line, while the run with ZEUS is shown as a dashed line. There is only a small difference between the outcomes visible here, although in the ZEUS run the magnetic energy density saturates at a slightly higher level.

One distinct feature of our sample nonlinear calculation is the formation of a density dip at center of the box. This dip can be clearly seen in the azimuthal and vertical averages of the density as a function of x, averaged for a period $t\Omega = 89.5 - 90.5$, as shown in the solid line of Figure 15. In order to improve signal to noise, we time average over 11 successive data dumps to generate this image. Across the radial grid, the magnitude of the density fluctuation is $\sim 0.1\rho_0$. This density dip has a width $\sim H$. Further investigations for the same test problem indicate that similar features appear in the results obtained with other algorithms such as the original ZEUS (shown in the dashed line of Figure 15) and ATHENA (Gardiner & Stone 2005; simulation kindly provided by J. Simon).

This density dip is a generic feature of large shearing box calculations. It is associated with large truncation errors generated by advecting fluid with respect to the

---

[1] This corresponds to the maximum growth rate in the magnetorotational instability (MRI; Balbus & Hawley 1991).

[2] Most shearing box simulations employ $L_x \sim H$, although some larger boxes have been run. Recent examples are $L_x = 8H$ (Papaloizou et al. 2004; Oishi et al. 2005; Papaloizou 2005; Piontek & Ostriker 2007), $16H$ (Kim & Ostriker 2006), $17H$ and $25H$ (Kim et al. 2002), although the latter two do not include the effects of the MRI.

[3] This version of ZEUS is available at Jim Stone's homepage `http://www.astro.princeton.edu/~ jstone/zeus.html`. We use this version in all our code comparison runs.

grid. These errors are not distributed evenly in the radial direction (Galilean invariance is not satisfied in an Eulerian integration with shear), therefore large variations in density appear in the center of the box because of the very small truncation error when $v \sim 0$. This problem is more severe for large boxes without orbital advection because the truncation errors increase as x increases. The variation in truncation error is relatively small over the range $|x| < H/2$, so this feature was not observed in earlier models with $L_x = H$.

For the magnetic field, this also means larger numerical diffusivity when $|x|$ increases. In Figure 16, we plot the radial distribution of the spatial averaged magnetic stress tensor, time averaged from $t = 89.5\Omega^{-1}$ to $t = 90.5\Omega^{-1}$. 11 data dumps are used to generate this image. Dissipation of the fields increases with $|x|$ and this leads to a gradual decrease of stress (as well as α) towards the boundary. At $x = \pm L_x/2$ the stress tensor drops to $\sim 50\%$ of its value at the center.

Notice the strong correlation between the peak of the stress tensor and the density dip. This is easy to understand because in a steady accretion disk $\alpha\Sigma$ is a constant, where Σ is the disk surface density. We have also observed that as the evolution time increases the magnitude of the density dip becomes larger due to the accumulation of truncation errors. For example, from $t = 40\Omega^{-1}$ to $t = 100\Omega^{-1}$ the $1st$ Fourier component a_1 of the density profile $a_1 = \int(\rho/\rho_0)\cos(2\pi k(x + L_x/2)/L_x)d^3x$ increases from ~ 0.005 to ~ 0.03. In a higher resolution study using a $N_x \times N_y \times N_z = 256 \times 256 \times 64$ box, a_1 runs from ~ 0.003 to ~ 0.02 over the same time; the feature persists, but decreases in magnitude, as the resolution increases.

The radial variation of truncation errors can be seen clearly in a linear magnetic field advection test using a large, radially extended box. In Figure 17 we plot azimuthally and vertically averaged errors in B_x as a function of x for an $L_x = 10H$ box. The alternate appearances of error minima and maxima are evident. Notice that in the orbital advection scheme, numerical errors are minimal at those locations x where the relative cell shift $S = -q\Omega x\Delta t/\Delta y$ is an integer, because no interpolation is needed. At the box center the fluid does not need to be shifted and the errors are minimal; as x increases, the relative shift gradually increases to $1/2$ and errors increase to a maximum; beyond this maximum the shift then decreases and errors reach a minimum again. The ith error minimum should appear at $x = x_i$ which satisfies $S = -q\Omega x_i\Delta t/\Delta y = i$, where i is an integer. In Figure 17 the error minima fall exactly at these locations.

For non-linear large box simulations, one prediction for the orbital advection scheme is that the density dip should appear at those locations where the cells are shifted by an integer amount. In the above $L_x = 8H$ model, the relative cell shift S in the orbital advection substep is always smaller than one, even at the radial boundary. We therefore perform an experiment by extending the radial size of the box to $32H$. For a size $L_x \times L_y \times L_z = 32H \times 2\pi H \times 2H$ box with a resolution $N_x \times N_y \times N_z = 1024 \times 64 \times 64$, the estimated time step is $\Delta t \sim 0.01\Omega^{-1}$ by assuming $|\Delta v| \sim 0.1c_s$. We then estimate that the first integer number shift should occur at $x_1 \sim \pm 7H$ and the second integer number shift should occur at $x_2 \sim \pm 14H$. In Figure 18, we plot the spatially averaged density as a function of x, averaged for a period $t\Omega = 90 - 100$ near the end of the run. The five density dips indeed show up at the predicted radial positions. It is a coincidence that the locations of the outer two density dips are close to the box edge. As shown in the above linear advection test, these locations are not controlled by the boundary conditions.

Future large scale shearing box calculations will need to eliminate or minimize the numerically induced radial variation in mean density. One way of reducing the magnitude of the dips is to give the whole box a large bulk epicyclic motion and let radial oscillations smooth out the errors. This may not be an ideal solution because any introduced large radial velocity will dramatically decrease the time step. A second approach is to simply shift the data by a few H in radius every few Ω^{-1}.

Finally, for larger shearing box simulations our scheme is more efficient than the original ZEUS. In the nonlinear stage of the sample calculation, our scheme is ~ 18 times faster on a Xeon 3.2GHz machine. Three factors contribute to this improved efficiency: (1) By using orbital advection the time step is controlled by Δv instead of v_{orb}. The Mach number of the flow with respect to a fixed grid at the outer edge of the sample model is 6, so the orbital advection scheme reduces the number of time steps by ~ 4.8; (2) We implement a larger time step than that used in the original ZEUS, which includes an unnecessary limit on the time step related to the size of the box. This reduces the number of time steps by another factor of ~ 2.6. For our sample non-linear calculation of size $L_x \times L_y \times L_z = 8H \times 8\pi H \times 2H$ box with a resolution $N_x \times N_y \times N_z = 256 \times 256 \times 64$, our time step is ~ 10 times larger than for ZEUS; (3) We use a simpler MOC-CT scheme than ZEUS does, which gives an additional factor of 1.3. The remaining factor of 1.1 is due to minor coding differences.

6. SUMMARY

We have developed a scheme for doing orbital advection of a magnetized fluid efficiently and accurately using interpolation. Our scheme is operator-split, and assumes that the magnetic field is discretized on a staggered mesh. The main difficulty we have overcome is interpolating the magnetic field in a way that preserves $\nabla \cdot \boldsymbol{B} = 0$. We note that other algorithms have been developed for interpolating magnetic fields in a divergence-free manner. For example, Balsara (2001) and Tóth & Roe (2002) provide prolongation and restriction formulas for interpolating fields between grids of different size in Adaptive Mesh Refinement codes. Our algorithm is distinct in that it is designed specifically for orbital advection.

Our algorithm can be implemented by encoding the finite difference expressions given by equations (21)-(30). The coefficients in these expressions are defined in Table A1. A version of the algorithm implemented in C is available at `http://rainman.astro.uiuc.edu/codelib`.[4] Our implementation of the algorithm performs orbital advection at the end of each time step. In principle, however, the orbital advection operator can be inserted

---

[4] Note that we absorb a factor of $1/2$ into the definition of the van Leer slopes in our code, which introduces a factor of 2 into some of the coefficients defined in Table A1.

at any point in the series of substeps that make up the numerical evolution. We have experimented with different insertion points for some of our tests and have seen no significant deviation from the results we present here. An important caveat is that the shearing box boundary conditions should always be applied at time t before the orbital advection substep, and at time $t + \Delta t$ after.

A sample shearing box calculation is shown in Figures 12-16 of the paper. Our scheme produces results entirely consistent with earlier shearing box calculations, but enables the simulation of larger shearing boxes more efficiently and more accurately. This should permit the study of structures with scales larger than $\sim H$ in local models of accretion disks.

One generic feature of these large shearing box simulations is the formation of density minima at $x \sim 0$ in the turbulent stage. We explored the origin of radial density variation and have shown that it originates from unevenly distributed truncation errors in the radial direction. Other numbrical algorithms, such as ZEUS and ATHENA, are subject to the same numerical artifact.

The idea behind orbital advections schemes (see also Masset 2000, Gammie 2001, and Johnson & Gammie 2005) is quite general. If (1) the fluid element orbits are known at the beginning of the time step (so the interpolation operator can be constructed), and (2) parts of the fluid are moving supersonically with respect to the grid (so that orbital advection removes the dominant part of the speed that enters the Courant condition) then one can in principal obtain a more efficient and more accurate evolution using orbital advection.

APPENDIX

A. FLUX CALCULATION

To fix ideas, consider first a given zone of the unsheared grid. For the Cartesian coordinate system we employ here, the total flux into the zone is given by

$$\Phi = \Phi x_{ijk} - \Phi x_{i+1jk} + \Phi y_{ijk} - \Phi y_{ij+1k} + \Phi z_{ijk} - \Phi z_{ijk+1}, \tag{A1}$$

where

$$\Phi x_{ijk} \equiv \Delta y \, \Delta z \int_{-1/2}^{1/2} dn_y \int_{-1/2}^{1/2} dn_z \, Bx(n_y, n_z), \tag{A2}$$

$$\Phi y_{ijk} \equiv \Delta x \, \Delta z \int_{-1/2}^{1/2} dn_x \int_{-1/2}^{1/2} dn_z \, By(n_x, n_z), \tag{A3}$$

and

$$\Phi z_{ijk} \equiv \Delta x \, \Delta y \int_{-1/2}^{1/2} dn_x \int_{-1/2}^{1/2} dn_y \, Bz(n_x, n_y).^5 \tag{A4}$$

The above integrals have been expressed in dimensionless zone units $n_x \equiv x/\Delta x$, $n_y \equiv y/\Delta y$, $n_z \equiv z/\Delta z$, and the integrands are a model for how the field components vary over a zone face. We choose a model that is second-order accurate in space:

$$Bx(n_y, n_z) \equiv bx_{ijk} + bx\_dqy_{ijk} \, n_y + bx\_dqz_{ijk} \, n_z, \tag{A5}$$

$$By(n_x, n_z) \equiv by_{ijk} + by\_dqx_{ijk} \, n_x + by\_dqz_{ijk} \, n_z, \tag{A6}$$

and

$$Bz(n_x, n_y) \equiv bz_{ijk} + bz\_dqx_{ijk} n_x + bz\_dqy_{ijk} n_y, \tag{A7}$$

where bx_{ijk}, by_{ijk} and bz_{ijk} are the face-centered components of the magnetic field in each zone and, e.g., bx_dqy_{ijk} is the van Leer slope of bx_{ijk} in the y direction (Stone & Norman 1992a). With these definitions for the field components, the total flux through a zone face in each orthogonal direction is given by

$$\Phi x_{ijk} = bx_{ijk} \, \Delta y \, \Delta z, \;\; \Phi y_{ijk} = by_{ijk} \, \Delta x \, \Delta z, \;\; \Phi z_{ijk} = bz_{ijk} \, \Delta x \, \Delta y. \tag{A8}$$

Using a subvolume bounded by zone faces from both the sheared grid and the new grid requires, in general, the calculation of fluxes through portions of the old grid faces. Figures 2-4 indicate the subfaces A_x, A_y and A_z over which the partial fluxes are defined, and the partial fluxes required for each of the three cases is given below:

$$\Phi xm1 \equiv \int_{A_{xm1}} dy \, dz \, Bx(y, z) = \Delta y \Delta z \int_{1/2-n_m}^{1/2} dn_y \int_{-1/2}^{1/2} dn_z \, Bx(n_y, n_z), \tag{A9}$$

$$\Phi xp1 \equiv \int_{A_{xp1}} dy \, dz \, Bx(y, z) = \Delta y \Delta z \int_{-1/2}^{-1/2+n_p} dn_y \int_{-1/2}^{1/2} dn_z \, Bx(n_y, n_z), \tag{A10}$$

---

[5] The magnetic field components are defined such that a positive value corresponds to a magnetic flux into the zone.

<div align="center">

TABLE 1
WEIGHT COEFFICIENTS

</div>

$w_{10} \equiv n_m$	$w_{18} \equiv \frac{1}{6}n_p^2(f+s)/s^2$	$w_{26} \equiv \frac{1}{2}\left(f - f^2 - s^2/12\right)$
$w_{11} \equiv \frac{1}{2}n_m(1 - n_m)$	$w_{19} \equiv \frac{1}{12}n_p^2(2n_p - 3)/s$	$w_{30} \equiv -n_m$
$w_{12} \equiv n_p$	$w_{20} \equiv n_m$	$w_{31} \equiv \frac{1}{2}n_m(1 + n_m)$
$w_{13} \equiv \frac{1}{2}n_p(n_p - 1)$	$w_{21} \equiv \frac{1}{2}n_m(1 - n_m)$	$w_{32} \equiv n_p$
$w_{14} \equiv \frac{1}{2}n_m^2/s$	$w_{22} \equiv -n_p$	$w_{33} \equiv \frac{1}{2}n_p(n_p - 1)$
$w_{15} \equiv \frac{1}{6}n_m^2(f - s)/s^2$	$w_{23} \equiv -\frac{1}{2}n_p(n_p + 1)$	$w_{34} \equiv -f$
$w_{16} \equiv \frac{1}{12}n_m^2(3 - 2n_m)/s$	$w_{24} \equiv f$	$w_{35} \equiv \frac{1}{12}s$
$w_{17} \equiv \frac{1}{2}n_p^2/s$	$w_{25} \equiv -\frac{1}{12}s$	$w_{36} \equiv \frac{1}{2}\left(f + f^2 + s^2/12\right)$

$$\Phi zm1 \equiv \int_{A_{zm1}} dx\, dy\, Bz(x,y) = \Delta x \Delta y \int_{-1/2}^{f/s} dn_x \int_{1/2-f+n_x s}^{1/2} dn_y\, Bz(n_x, n_y), \tag{A11}$$

$$\Phi zp1 \equiv \int_{A_{zp1}} dx\, dy\, Bz(x,y) = \Delta x \Delta y \int_{f/s}^{1/2} dn_x \int_{-1/2}^{-1/2-f+n_x s} dn_y\, Bz(n_x, n_y), \tag{A12}$$

$$\Phi xm2 \equiv \int_{A_{xm2}} dy\, dz\, Bx(y,z) = \Delta y \Delta z \int_{1/2-n_m}^{1/2} dn_y \int_{-1/2}^{1/2} dn_z\, Bx(n_y, n_z), \tag{A13}$$

$$\Phi xp2 \equiv \int_{A_{xp2}} dy\, dz\, Bx(y,z) = \Delta y \Delta z \int_{1/2+n_p}^{1/2} dn_y \int_{-1/2}^{1/2} dn_z\, Bx(n_y, n_z), \tag{A14}$$

$$\Phi z2 \equiv \int_{A_{z2}} dx\, dy\, Bz(x,y) = \Delta x \Delta y \int_{-1/2}^{1/2} dn_x \int_{1/2-f+n_x s}^{1/2} dn_y\, Bz(n_x, n_y), \tag{A15}$$

$$\Phi xm3 \equiv \int_{A_{xm3}} dy\, dz\, Bx(y,z) = \Delta y \Delta z \int_{-1/2}^{-1/2-n_m} dn_y \int_{-1/2}^{1/2} dn_z\, Bx(n_y, n_z), \tag{A16}$$

$$\Phi xp3 \equiv \int_{A_{xp3}} dy\, dz\, Bx(y,z) = \Delta y \Delta z \int_{-1/2}^{-1/2+n_p} dn_y \int_{-1/2}^{1/2} dn_z\, Bx(n_y, n_z), \tag{A17}$$

$$\Phi z3 \equiv \int_{A_{z3}} dx\, dy\, Bz(x,y) = \Delta x \Delta y \int_{-1/2}^{1/2} dn_x \int_{-1/2}^{-1/2-f+n_x s} dn_y\, Bz(n_x, n_y), \tag{A18}$$

where m and p denote subfaces towards $x = -L_x/2$ and $x = +L_x/2$, respectively (to the right and left in Figures 2-4), the fluxes are numbered according to the case for which they are relevant, and the dimensionless zone lengths

$$n_m \equiv \frac{s}{2} + f, \quad n_p \equiv \frac{s}{2} - f \tag{A19}$$

are proportional to the azimuthal dimensions of A_{xm} and A_{xp}, respectively.[6]

Using the model defined by equations (A5) through (A7), the partial fluxes are given are given by

$$\Phi xm1_{ijk} = \Delta y \Delta z\, (w_{10}\, bx_{ijk} + w_{11}\, bx\_dqy_{ijk}), \tag{A20}$$

$$\Phi xp1_{ijk} = \Delta y \Delta z\, (w_{12}\, bx_{ijk} + w_{13}\, bx\_dqy_{ijk}), \tag{A21}$$

$$\Phi zm1_{ijk} = \Delta x \Delta y\, (w_{14}\, bz_{ijk} + w_{15}\, bz\_dqx_{ijk} + w_{16}\, bz\_dqy_{ijk}), \tag{A22}$$

$$\Phi zp1_{ijk} = \Delta x \Delta y\, (w_{17}\, bz_{ijk} + w_{18}\, bz\_dqx_{ijk} + w_{19}\, bz\_dqy_{ijk}), \tag{A23}$$

$$\Phi xm2_{ijk} = \Delta y \Delta z\, (w_{20}\, bx_{ijk} + w_{21}\, bx\_dqy_{ijk}), \tag{A24}$$

$$\Phi xp2_{ijk} = \Delta y \Delta z\, (w_{22}\, bx_{ijk} + w_{23}\, bx\_dqy_{ijk}), \tag{A25}$$

$$\Phi z2_{ijk} = \Delta x \Delta y\, (w_{24}\, bz_{ijk} + w_{25}\, bz\_dqx_{ijk} + w_{26}\, bz\_dqy_{ijk}), \tag{A26}$$

$$\Phi xm3_{ijk} = \Delta y \Delta z\, (w_{30}\, bx_{ijk} + w_{31}\, bx\_dqy_{ijk}), \tag{A27}$$

[6] The origin of the coordinate system for these integrals is defined to be at the location of the field component over which the integral is being performed. The integral is over the field in a sheared zone, so that the coordinate axes are parallel to the y, z and *sheared x* directions (the latter axes are indicated by dotted lines in Figures 2-4). One can think of an integral over a portion of an x-y subface (e.g., A_{zm1}) in the following manner. Imagine the "volume" under the $Bz(n_x, n_y)$ surface as a series of infinitesimal slabs of length 1 and width dn_x (in dimensionless zone units) stacked side-by-side in the radial direction. Integration over n_y yields the infinitesimal volume of one of these slabs, and a subsequent integration over n_x yields the total volume under the $Bz(n_x, n_y)$ surface. It is important to perform the integrals in the direction of increasing x, y and z so as not to introduce sign errors in the calculation of the fluxes.

$$\Phi xp3_{ijk} = \Delta y \Delta z \left(w_{32} \, bx_{ijk} + w_{33} \, bx\_dqy_{ijk} \right), \tag{A28}$$

$$\Phi z3_{ijk} = \Delta x \Delta y \left(w_{34} \, bz_{ijk} + w_{35} \, bz\_dqx_{ijk} + w_{36} \, bz\_dqy_{ijk} \right), \tag{A29}$$

where the coefficients w depend only on the index i (via f) and are defined in Table A1.

Using Figures 2-4 as a guide, these definitions can be used to map the sheared grid onto the new grid. The update of each magnetic field component can be treated as an independent calculation, although in practice it is natural to perform the azimuthal update first, since the updated azimuthal field depends upon the old values for all three components.

Radial Magnetic Field

The radial flux through a new zone is simply given by the sum of the radial fluxes through the portions of the old zones that overlay the new grid. Based upon Figures 2-4, the updated radial flux for each case is given by
Case 1:

$$\Phi x_{ijk}^{n+1} = \Phi x_{iJk}^{n} - \Phi xm1_{iJk}^{n} + \Phi xm1_{iJ-1k}^{n}, \tag{A30}$$

Case 2:

$$\Phi x_{ijk}^{n+1} = \Phi x_{iJk}^{n} - \Phi xm2_{iJk}^{n} + \Phi xm2_{iJ-1k}^{n}, \tag{A31}$$

Case 3:

$$\Phi x_{ijk}^{n+1} = \Phi x_{iJk}^{n} - \Phi xm3_{iJk}^{n} + \Phi xm3_{iJ+1k}^{n}. \tag{A32}$$

Converting fluxes to magnetic field components via definitions (A20), (A24) and (A27) yields the final expressions given in the text (equations [21]-[23]).

Azimuthal Magnetic Field

Calculation of the azimuthal field component is the most complicated and requires explicit use of the divergence-free constraint. The choice of subvolume over which to sum the fluxes in a manner consistent with this constraint is not unique, so we construct the algorithm under the additional considerations of spatial symmetry and accuracy.
Case 1:

We consider three subvolumes for Case 1, indicated by the dark and light shaded regions in Figure 2 and the region bounded above and below by A_{zm1} and A_{zp1}. Summing the fluxes out of the upper (light shaded) subvolume gives

$$-\Phi y_{ijk}^{n+1} + \Phi y_{iJ+1k}^{n} - \Phi xm1_{iJ-1k}^{n} - \Phi x_{iJk}^{n}$$
$$+ \Phi x_{i+1Jk}^{n} - \Phi xp1_{i+1Jk}^{n} + \Phi zm1_{iJ-1k+1}^{n} - \Phi zm1_{iJ-1k}^{n}$$
$$+ \Phi z_{iJk+1}^{n} - \Phi zp1_{iJk+1}^{n} - \Phi z_{iJk}^{n} + \Phi zp1_{iJk}^{n} = 0. \tag{A33}$$

Summing the fluxes into the lower (dark shaded) subvolume gives

$$-\Phi y_{ijk}^{n+1} + \Phi y_{iJ-1k}^{n} + \Phi x_{iJ-1k}^{n} - \Phi xm1_{iJ-1k}^{n} - \Phi x_{i+1J-1k}^{n}$$
$$- \Phi xp1_{i+1Jk}^{n} - \Phi z_{iJ-1k+1}^{n} + \Phi zm1_{iJ-1k+1}^{n}$$
$$+ \Phi z_{iJ-1k}^{n} - \Phi zm1_{iJ-1k}^{n} - \Phi zp1_{iJk+1}^{n} + \Phi zp1_{iJk}^{n} = 0. \tag{A34}$$

Summing the fluxes out of the region bounded above and below by A_{zm1} and into the region bounded above and below by A_{zp1} gives

$$-\Phi y_{ijk}^{n+1} + \Phi y_{iJk}^{n} - \Phi xm1_{iJ-1k}^{n} - \Phi xp1_{i+1Jk}^{n}$$
$$+ \Phi zm1_{iJ-1k+1}^{n} - \Phi zm1_{iJ-1k}^{n} + \Phi zp1_{iJk}^{n} - \Phi zp1_{iJk+1}^{n} = 0. \tag{A35}$$

Averaging expressions (A33) and (A34) gives the most symmetric algorithm, but the smaller stencil of expression (A35) results in less divergence. The optimum algorithm is therefore to alternate every other time step between the average of expressions (A33) and (A35) and the average of expressions (A34) and (A35).
Case 1 (n even):

$$\Phi y_{ijk}^{n+1} = (1/2) \left[\Phi y_{iJk}^{n} + \Phi y_{iJ+1k}^{n} - 2\,\Phi xm1_{iJ-1k}^{n} - \Phi x_{iJk}^{n} \right.$$
$$+ \Phi x_{i+1Jk}^{n} - 2\,\Phi xp1_{i+1Jk}^{n} + 2\,\Phi zm1_{iJ-1k+1}^{n} - 2\,\Phi zm1_{iJ-1k}^{n}$$
$$\left. + \Phi z_{iJk+1}^{n} - 2\,\Phi zp1_{iJk+1}^{n} - \Phi z_{iJk}^{n} + 2\,\Phi zp1_{iJk}^{n} \right]. \tag{A36}$$

Case 1 (n odd):

$$\Phi y_{ijk}^{n+1} = (1/2) \left[\Phi y_{iJk}^{n} + \Phi y_{iJ-1k}^{n} + \Phi x_{iJ-1k}^{n} - 2\,\Phi xm1_{iJ-1k}^{n} - \Phi x_{i+1J-1k}^{n} \right.$$
$$- 2\,\Phi xp1_{i+1Jk}^{n} - \Phi z_{iJ-1k+1}^{n} + 2\,\Phi zm1_{iJ-1k+1}^{n}$$
$$\left. + \Phi z_{iJ-1k}^{n} - 2\,\Phi zm1_{iJ-1k}^{n} - 2\,\Phi zp1_{iJk+1}^{n} + 2\,\Phi zp1_{iJk}^{n} \right]. \tag{A37}$$

Converting fluxes to magnetic field components via definitions (A20)-(A23) yields the final expressions given in the text (equations [24] and [25]).

Case 2:

We consider two subvolumes for Case 2, indicated by the dark and light shaded regions in Figure 3. Summing the fluxes out of the upper (light shaded) subvolume gives

$$
-\Phi y_{ijk}^{n+1} + \Phi y_{iJk}^n - \Phi xm2_{iJ-1k}^n + \Phi xp2_{i+1J-1k}^n
$$
$$
+ \Phi z2_{iJ-1k+1}^n - \Phi z2_{iJ-1k}^n = 0, \tag{A38}
$$

whereas summing the fluxes into the lower (dark shaded) subvolume gives

$$
-\Phi y_{ijk}^{n+1} + \Phi y_{iJ-1k}^n + \Phi x_{iJ-1k}^n - \Phi xm2_{iJ-1k}^n - \Phi x_{i+1J-1k}^n + \Phi xp2_{i+1J-1k}^n
$$
$$
- \Phi z_{iJ-1k+1}^n + \Phi z2_{iJ-1k+1}^n + \Phi z_{iJ-1k}^n - \Phi z2_{iJ-1k}^n = 0. \tag{A39}
$$

Taking the average of expressions (A38) and (A39) gives

$$
\Phi y_{ijk}^{n+1} = (1/2) \left[\Phi y_{iJk}^n + \Phi y_{iJ-1k}^n \right.
$$
$$
+ \Phi x_{iJ-1k}^n - 2\,\Phi xm2_{iJ-1k}^n - \Phi x_{i+1J-1k}^n + 2\,\Phi xp2_{i+1J-1k}^n
$$
$$
\left. - \Phi z_{iJ-1k+1}^n + 2\,\Phi z2_{iJ-1k+1}^n) + \Phi z_{iJ-1k}^n - 2\,\Phi z2_{iJ-1k}^n \right]. \tag{A40}
$$

Converting fluxes to magnetic field components via definitions (A24)-(A26) yields the final expression given in the text (equation [26]).

Case 3:

This case, shown in Figure 4, is the mirror image of Case 2. Summing the fluxes out of the upper (light shaded) subvolume gives

$$
-\Phi y_{ijk}^{n+1} + \Phi y_{iJ+1k}^n - \Phi x_{iJk}^n + \Phi xm3_{iJk}^n
$$
$$
+ \Phi x_{i+1Jk}^n - \Phi xp3_{i+1Jk}^n + \Phi z_{iJk+1}^n - \Phi z3_{iJk+1}^n - \Phi z_{iJk}^n + \Phi z3_{iJk}^n = 0, \tag{A41}
$$

whereas summing the fluxes into the lower (dark shaded) subvolume gives

$$
-\Phi y_{ijk}^{n+1} + \Phi y_{iJk}^n + \Phi xm3_{iJk}^n - \Phi xp3_{i+1Jk}^n
$$
$$
- \Phi z3_{iJk+1}^n + \Phi z3_{iJk}^n = 0. \tag{A42}
$$

Taking the average of expressions (A41) and (A42) gives

$$
\Phi y_{ijk}^{n+1} = (1/2) \left[\Phi y_{iJk}^n + \Phi y_{iJ+1k}^n \right.
$$
$$
- \Phi x_{iJk}^n + 2\,\Phi xm3_{iJk}^n + \Phi x_{i+1Jk}^n - 2\,\Phi xp3_{i+1Jk}^n
$$
$$
\left. + \Phi z_{iJk+1}^n - 2\,\Phi z3_{iJk+1}^n - \Phi z_{iJk}^n + 2\,\Phi z3_{iJk}^n \right]. \tag{A43}
$$

Converting fluxes to magnetic field components via definitions (A27)-(A29) yields the final expression given in the text (equation [27]).

Vertical Magnetic Field

The calculation for the vertical field component proceeds in a manner similar to that for the radial component. The updated vertical flux for each case is given by

Case 1:

$$
\Phi z_{ijk}^{n+1} = \Phi z_{iJk}^n - \Phi zm1_{iJk}^n + \Phi zm1_{iJ-1k}^n + \Phi zp1_{iJ+1k}^n - \Phi zp1_{iJk}^n, \tag{A44}
$$

Case 2:

$$
\Phi z_{ijk}^{n+1} = \Phi z_{iJk}^n - \Phi z2_{iJk}^n + \Phi z2_{iJ-1k}^n, \tag{A45}
$$

Case 3:

$$
\Phi z_{ijk}^{n+1} = \Phi z_{iJk}^n - \Phi z3_{iJk}^n + \Phi z3_{iJ+1k}^n. \tag{A46}
$$

Converting fluxes to magnetic field components via definitions (A22), (A26) and (A29) yields the final expressions given in the text (equations [28]-[30]).

B. SHEARING WAVE TESTS

We use the analytical solutions outlined by Johnson (2007) as the initial conditions for the linear tests in §4 (Figures 8-11). The incompressive solution is given by the real parts of expressions (80)-(82) of that paper. For imaginary ω and $\tilde{\omega}$ and a Keplerian rotation profile, these are

$$
\delta \boldsymbol{v} = \delta \tilde{\boldsymbol{v}} \cos\left(\boldsymbol{k} \cdot \boldsymbol{x} + \frac{\pi}{4} \right) \tag{B1}
$$

and

$$
\delta \boldsymbol{v}_A = \delta \tilde{\boldsymbol{v}}_A \cos\left(\boldsymbol{k} \cdot \boldsymbol{x} - \frac{\pi}{4} \right), \tag{B2}
$$

with

$$\delta\tilde{\boldsymbol{v}} = \mathcal{A}_i \left(k_x^2 - k^2, k_x k_y - \frac{k^2}{2\alpha}, k_x k_z + \frac{k^2 k_y}{2\alpha k_z} \right) \tag{B3}$$

and

$$\delta\tilde{\boldsymbol{v}}_A = -\frac{\boldsymbol{v}_A \cdot \boldsymbol{k}}{|\omega|} \mathcal{A}_i \left(k_x^2 - k^2, k_x k_y + 2\alpha k_z^2, k_x k_z - 2\alpha k_y k_z \right), \tag{B4}$$

where

$$\mathcal{A}_i = \epsilon c_s H \frac{|\tilde{\omega}|}{\Omega} \sqrt{\frac{|\omega|\Omega}{2|\tilde{\omega}^2|k^2 + \Omega^2 k_z^2}}, \tag{B5}$$

$$\alpha = \frac{\Omega|\omega|}{|\tilde{\omega}^2|}, \tag{B6}$$

and ϵ is an arbitrary perturbation amplitude. These expressions have been normalized to the correct dimensional units. The density perturbation is given by

$$\frac{\delta\rho}{\rho_0} = \frac{\tilde{\delta\rho}}{\rho_0} \cos\left(\boldsymbol{k} \cdot \boldsymbol{x} - \frac{\pi}{4}\right), \tag{B7}$$

with

$$\frac{\tilde{\delta\rho}}{\rho_0} = \left(-\frac{\boldsymbol{v}_A}{c_s} \cdot \frac{\delta\tilde{\boldsymbol{v}}_A}{c_s} + \frac{2\Omega}{c_s k} \left[\frac{k_x}{k}\hat{\boldsymbol{y}} + \frac{k_y}{2k}\hat{\boldsymbol{x}} \right] \cdot \frac{\delta\tilde{\boldsymbol{v}}}{c_s} \right). \tag{B8}$$

The unstable branch of the incompressive dispersion relation is

$$|\tilde{\omega}^2| = \left(\frac{k_z \Omega}{k} \right)^2 \left(\sqrt{1 + \left[\frac{4k \boldsymbol{v}_A \cdot \boldsymbol{k}}{k_z \Omega} \right]^2} - 1 \right) \tag{B9}$$

and

$$|\omega| = \sqrt{|\tilde{\omega}^2| - (\boldsymbol{v}_A \cdot \boldsymbol{k})^2}. \tag{B10}$$

For our choice of initial parameters, $\boldsymbol{v}_A = \sqrt{15/16}(\Omega/k_z)\hat{\boldsymbol{z}}$ and $H\boldsymbol{k} = 2\pi(-2/10, 1/10, 1)$, these become

$$|\tilde{\omega}^2| = \Omega^2 \frac{5}{21} \left(\sqrt{67} - 2 \right) \simeq 1.47\Omega^2 \tag{B11}$$

and

$$|\omega| = \Omega\sqrt{\frac{5}{21}} \left(\sqrt{67} - \frac{95}{16} \right)^{1/2} \simeq 0.732\Omega. \tag{B12}$$

The perturbations in this limit are given by

$$\delta\tilde{\boldsymbol{v}} = -\frac{\mathcal{A}_i}{H^2} (2\pi)^2 \left(\frac{101}{100}, \frac{1}{50} + \frac{21}{40\alpha}, \frac{1}{5} - \frac{21}{400\alpha} \right) \tag{B13}$$

and

$$\delta\tilde{\boldsymbol{v}}_A = \sqrt{\frac{15}{16}} \frac{\Omega}{|\omega|} \frac{\mathcal{A}_i}{H^2} (2\pi)^2 \left(\frac{101}{100}, \frac{1}{50} - 2\alpha, \frac{1}{5} + \frac{\alpha}{5} \right), \tag{B14}$$

with

$$\frac{\mathcal{A}_i}{H^2} = \epsilon c_s \frac{|\omega|}{2\pi\Omega} \left(\frac{2}{\alpha\sqrt{67}} \right)^{1/2} \tag{B15}$$

and

$$\alpha = \frac{\sqrt{21}\left(\sqrt{67} - 95/16\right)^{1/2}}{\sqrt{5}\left(\sqrt{67} - 2\right)} \simeq 0.497. \tag{B16}$$

Dividing through by an overall factor of $H^2(k_x^2 - k^2) = -(2\pi)^2(101/100)$ gives the initial conditions quoted above (with $\epsilon = 10^{-6}$ and $c_s = \Omega = \rho_0 = 1$).

We make comparisons based upon the amplitude of the solution, i.e. $\delta\tilde{\boldsymbol{v}}$ and $\delta\tilde{\boldsymbol{v}}_A$ rather than $\delta\boldsymbol{v}$ and $\delta\boldsymbol{v}_A$. In Figures 8-10, then, the quantity that is being plotted is $\delta\tilde{\boldsymbol{v}}^2 + \delta\tilde{\boldsymbol{v}}_A^2$. To extract these quantities from the code, we perform spatial sine and cosine Fourier transforms in shearing coordinates on each of the velocity and magnetic field

components, and sum the squares of the transforms. As a concrete example, the cosine transform of the radial velocity component at time step t^n is given by

$$\delta \tilde{v}_x(t^n) = \frac{2}{N_x N_y N_z} \sum_{i=1}^{N_x} \sum_{j=1}^{N_y} \sum_{k=1}^{N_z} vx_{ijk}^n \cos\left(\boldsymbol{k}[t^n] \cdot \boldsymbol{x}_{ijk}\right), \tag{B17}$$

where $\boldsymbol{k}(t) = \boldsymbol{k}(0) + q\Omega k_y t\hat{\boldsymbol{x}}$. Since the solution as expressed above breaks down as ω transitions from imaginary to real, we calculate the analytical amplitudes for the incompressive tests based upon an integration of the full set of linear equations.[7]

The compressive solution is given by the real part of expressions (83)-(85) of Johnson (2007):

$$(\delta \boldsymbol{v}, \delta \boldsymbol{v}_A, \delta \rho) = \left(\tilde{\delta \boldsymbol{v}}, \tilde{\delta \boldsymbol{v}}_A, \tilde{\delta \rho}\right) \cos\left(\boldsymbol{k} \cdot \boldsymbol{x}\right), \tag{B18}$$

with

$$\tilde{\delta \boldsymbol{v}} = \frac{\omega}{\tilde{\omega}}\mathcal{A}_c \left(\frac{\omega^2}{k^2}\boldsymbol{k} - \boldsymbol{v}_A \cdot \boldsymbol{k}\, \boldsymbol{v}_A\right), \tag{B19}$$

$$\tilde{\delta \boldsymbol{v}}_A = \frac{\omega^2}{\tilde{\omega}}\mathcal{A}_c \left(\boldsymbol{v}_A - \frac{\boldsymbol{v}_A \cdot \boldsymbol{k}}{k^2}\boldsymbol{k}\right), \tag{B20}$$

and

$$\frac{\tilde{\delta \rho}}{\rho_0} = \tilde{\omega}\mathcal{A}_c, \tag{B21}$$

where

$$\mathcal{A}_c = \epsilon Hk\sqrt{\frac{\omega\Omega}{\omega^4 - (\boldsymbol{v}_A \cdot \boldsymbol{k})^2 c_s^2 k^2}}. \tag{B22}$$

Our choice of initial parameters for this test, $\boldsymbol{v}_A = c_s(0.1, 0.2, 0.0)$ and $H\boldsymbol{k} = 4\pi(-2, 1, 1)$, gives $\boldsymbol{v}_A \cdot \boldsymbol{k} = 0$, so that the nonzero solution to the compressive dispersion relation is

$$\omega^2 = \left(c_s^2 + v_A^2\right) k^2. \tag{B23}$$

The perturbations in this limit are given by

$$\left(\tilde{\delta \boldsymbol{v}}, \tilde{\delta \boldsymbol{v}}_A, \frac{\tilde{\delta \rho}}{\rho_0}\right) = \epsilon \left(v_A\sqrt{1+\beta}\,\hat{\boldsymbol{k}}, \boldsymbol{v}_A, 1\right) \left(Hk\sqrt{\frac{\beta}{1+\beta}}\right)^{1/2}, \tag{B24}$$

where $\beta = c_s^2/v_A^2$. For our initial conditions ($\beta = 20$), this is

$$\left(\tilde{\delta \boldsymbol{v}}, \tilde{\delta \boldsymbol{v}}_A, \frac{\tilde{\delta \rho}}{\rho_0}\right) = \epsilon \left(\frac{c_s}{2}\sqrt{\frac{7}{10}}\frac{H\boldsymbol{k}}{4\pi}, \boldsymbol{v}_A, 1\right) \left(8\pi\sqrt{\frac{10}{7}}\right)^{1/2}, \tag{B25}$$

which matches the numbers given above (with $\epsilon = 10^{-6}$ and $c_s = \Omega = \rho_0 = 1$).

Figure 11 shows the evolution of the azimuthal component of $\delta \tilde{\boldsymbol{v}}_A$. The numerical results are

$$\left(\delta \tilde{v}_{Ay}[t^n]\right)_{numerical} = \frac{2}{N_x N_y N_z} \sum_{i=1}^{N_x} \sum_{j=1}^{N_y} \sum_{k=1}^{N_z} \left(\frac{by_{ijk}^n}{\sqrt{4\pi\rho_0}} - v_{Ay}[t^n]\right) \cos\left(\boldsymbol{k}[t^n] \cdot \boldsymbol{x}_{ijk}\right). \tag{B26}$$

and the analytical results are calculated within the code using the time dependent version of expression (B25), i.e.

$$\left(\delta \tilde{v}_{Ay}[t^n]\right)_{analytical} = v_{Ay}[t^n] \left(8\pi\sqrt{\frac{10}{7}}\right)^{1/2} \cos\left(\sum_{n'=0}^{n} \omega[t^{n'}]\, dt^{n'}\right), \tag{B27}$$

with $dt^0 = 0$.

As a final practical consideration, implementing the solutions as described above can introduce divergence into the initial conditions. To avoid this, we calculate the vector potential in the Coulomb guage ($\boldsymbol{k} \cdot \delta \boldsymbol{A} = 0$) for the above solutions and numerically calculate its curl to obtain the initial magnetic field perturbation. The perturbed vector potential is

$$\frac{\delta \boldsymbol{A}}{\sqrt{4\pi\rho_0}} = -\frac{\boldsymbol{v}_A \cdot \boldsymbol{k}}{|\omega|}\mathcal{A}_i k_z \left(2\alpha\left[\frac{k_x^2}{k^2} - 1\right], 2\alpha\frac{k_x k_y}{k^2} - 1, 2\alpha\frac{k_x k_z}{k^2} + \frac{k_y}{k_z}\right) \cos\left(\boldsymbol{k} \cdot \boldsymbol{x} + \frac{\pi}{4}\right) \tag{B28}$$

---

[7] A copy of this code is available at http://rainman.astro.uiuc.edu/codelib.

for the incompressive solution and

$$\frac{\delta \boldsymbol{A}}{\sqrt{4\pi\rho_0}} = \frac{\omega^2 \boldsymbol{v}_A \times \boldsymbol{k}}{\tilde{\omega} k^2} \mathcal{A}_c \sin\left(\boldsymbol{k} \cdot \boldsymbol{x}\right) \tag{B29}$$

for the compressive solution. For our initial conditions, these reduce to

$$\frac{\delta \boldsymbol{A}}{\sqrt{4\pi\rho_0}} = \epsilon \frac{c_s H}{14} \left(\frac{1}{30\alpha\sqrt{67}}\right)^{1/2} \left(202\alpha, 4\alpha + 105, 40\alpha - \frac{21}{2}\right) \cos\left(\boldsymbol{k} \cdot \boldsymbol{x} + \frac{\pi}{4}\right) \tag{B30}$$

for the incompressive solution (with α given by expression [B16]), and

$$\frac{\delta \boldsymbol{A}}{\sqrt{4\pi\rho_0}} = \epsilon \frac{c_s H}{60} \left(\frac{1}{\pi}\sqrt{\frac{5}{14}}\right)^{1/2} (2, -1, 5) \sin\left(\boldsymbol{k} \cdot \boldsymbol{x}\right) \tag{B31}$$

for the compressive solution.

REFERENCES

Balbus, S. A., & Hawley, J. F. 1991, ApJ, 376, 214

Balsara, D. S. 2001, Journal of Computational Physics, 174, 614

Caunt, S. E., & Korpi, M. J. 2001, A&A, 369, 706

Gammie, C. F. 2001, ApJ, 553, 174

Gardiner, T. A., & Stone, J. M. 2005, Journal of Computational Physics, 205, 509

Hawley, J. F., Gammie, C. F., & Balbus, S. A. 1995, ApJ, 440, 742

Johnson, B. M., & Gammie, C. F. 2003, ApJ, 597, 131

Johnson, B. M., & Gammie, C. F. 2005, ApJ, 635, 149

Johnson, B. M. 2007,ApJ, 660,1374

Kim, W.-T., Ostriker, E. C., & Stone, J. M. 2002, ApJ, 581, 1080

Kim, W.-T., & Ostriker, E. C. 2006, ApJ, 646, 213

Masset, F. 2000, A&AS, 141, 165

Oishi, J. S., Mac Low, M. M.& Menou, K. 2005, prpl.conf.84390

Papaloizou, J. C. B., Nelson, R. P., & Snellgrove, M. D. 2004, MNRAS, 350, 829

Papaloizou, J. C. B. 2005, Celestial Mechanics and Dynamical Astronomy, 91, 33

Piontek, R. A. & Ostriker, E. C. 2007, ApJ, 663, 183

Stone, J. M. & Norman, M. L. 1992, ApJS, 80, 753

Stone, J. M. & Norman, M. L. 1992, ApJS, 80, 791

Tóth, G., & Roe, P. L. 2002, Journal of Computational Physics, 180, 736

Umurhan, O. M., & Regev, O. 2004, A&A, 427, 855
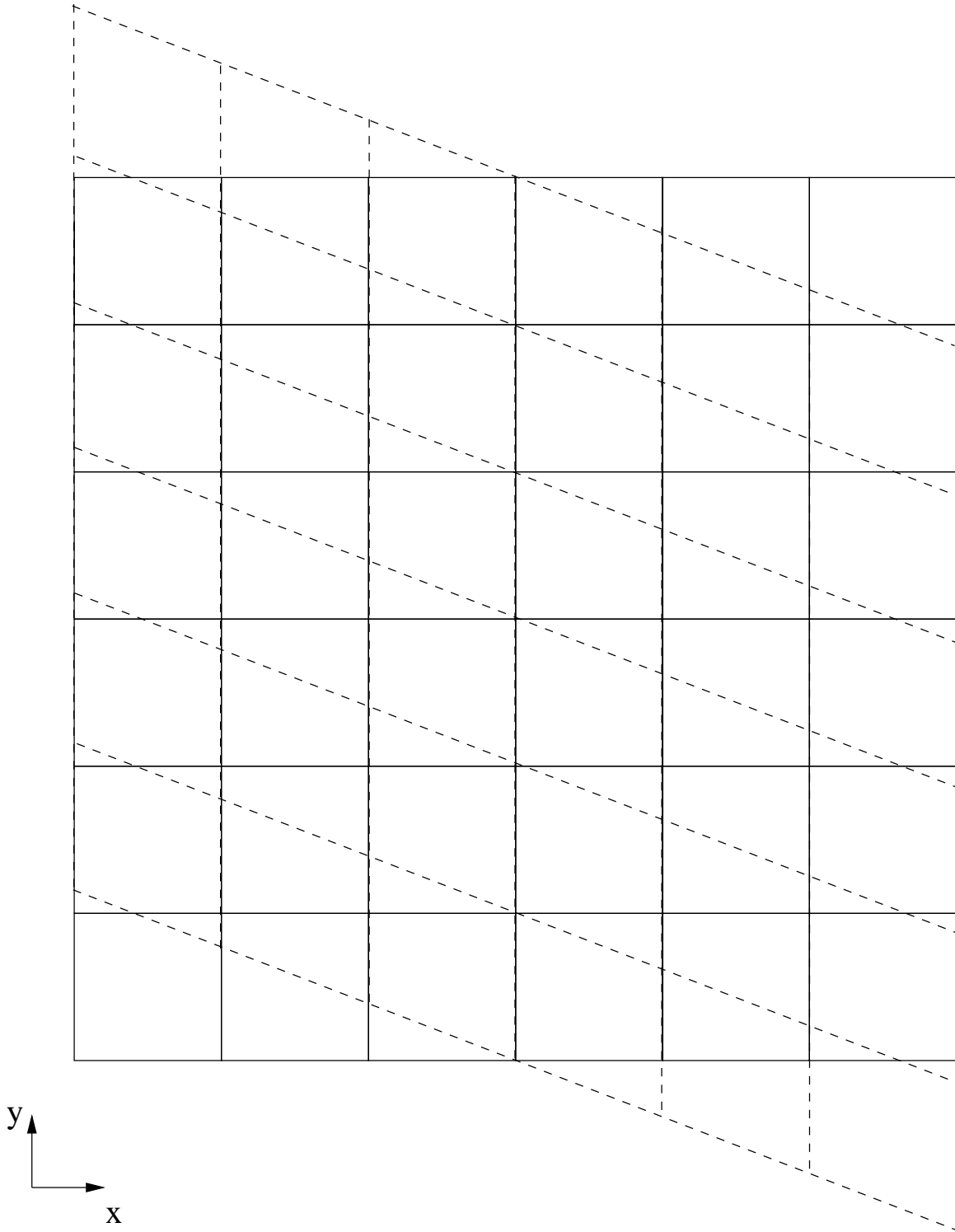
FIG. 1.— The effect of the background shear flow on a Cartesian grid. The dashed lines represent the old grid after it has been distorted by the shear, and the solid lines represent a new grid onto which the sheared grid is to be mapped.
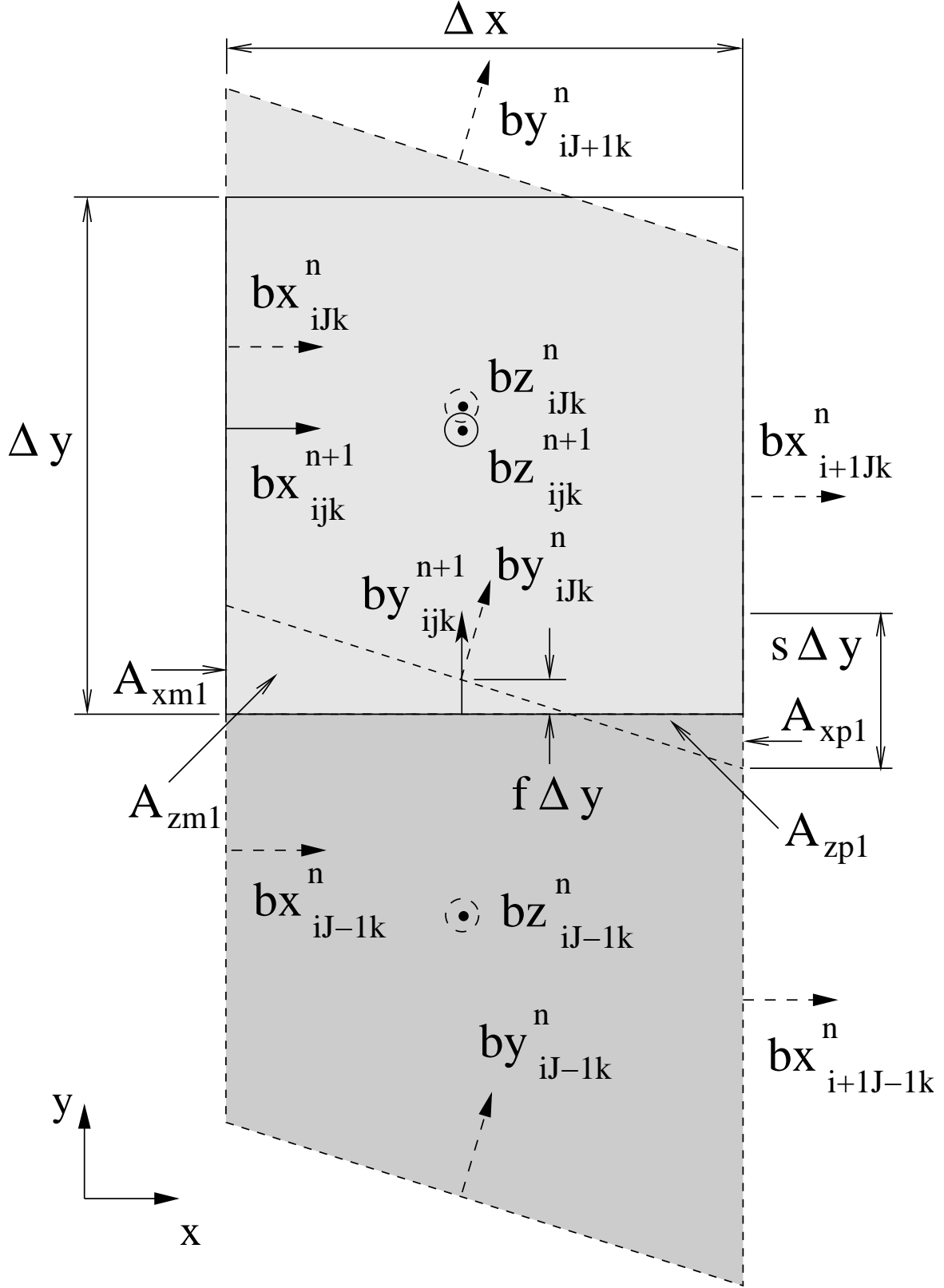
Fig. 2.— A slice in the $x - y$ plane for the Case 1 remap. The dashed lines represent the old grid (n) after it has been distorted by the shear, and the solid square is a new grid zone $(n + 1)$ onto which the fluxes are to be mapped. The shaded regions correspond to subvolumes over which the fluxes are summed for the remap of the azimuthal field. See Appendix A for definitions.
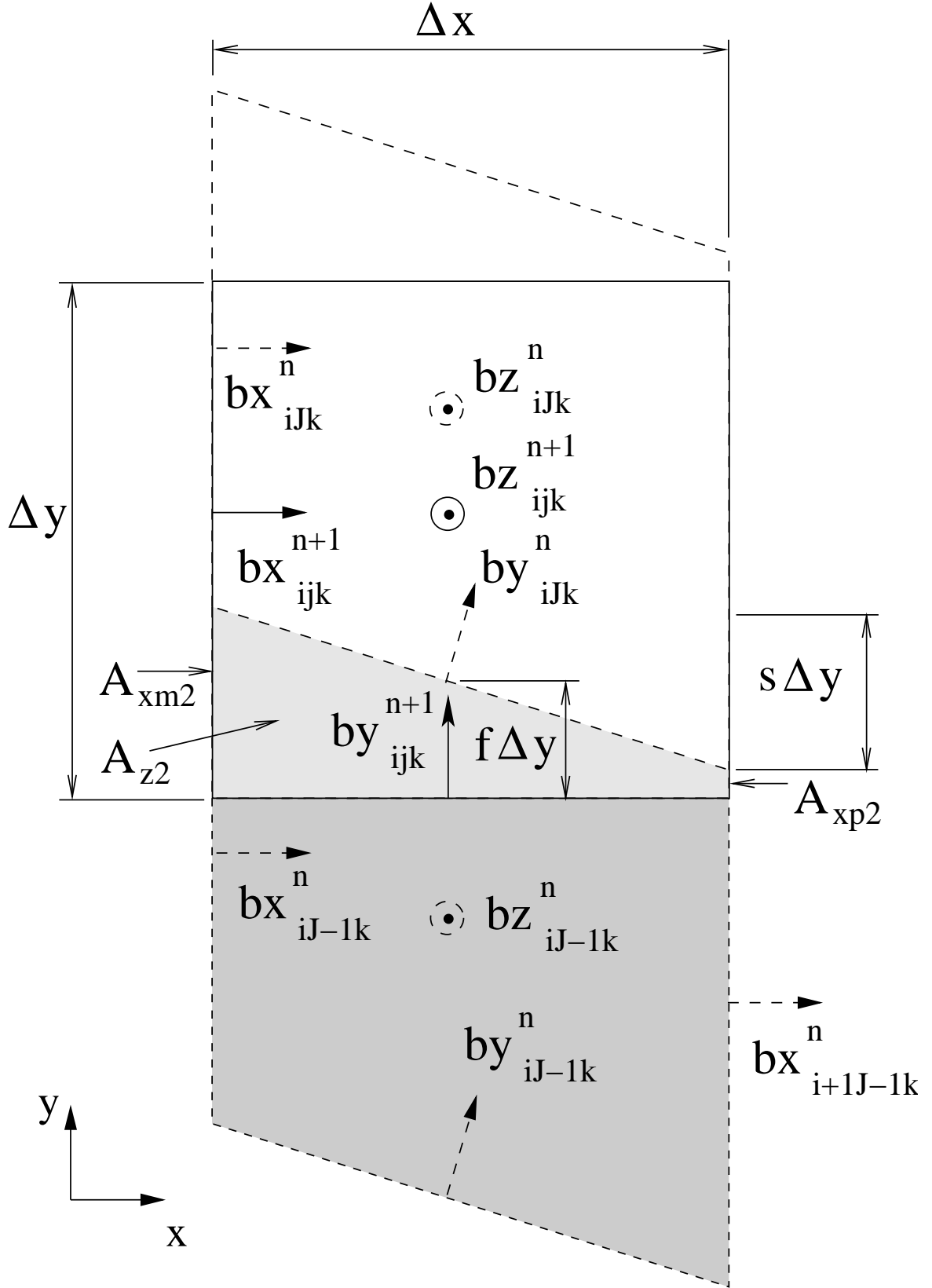
FIG. 3.— A slice in the $x - y$ plane for the Case 2 remap. The dashed lines represent the old grid (n) after it has been distorted by the shear, and the solid square is a new grid zone ($n + 1$) onto which the fluxes are to be mapped. The shaded regions correspond to subvolumes over which the fluxes are summed for the remap of the azimuthal field. See Appendix A for definitions.
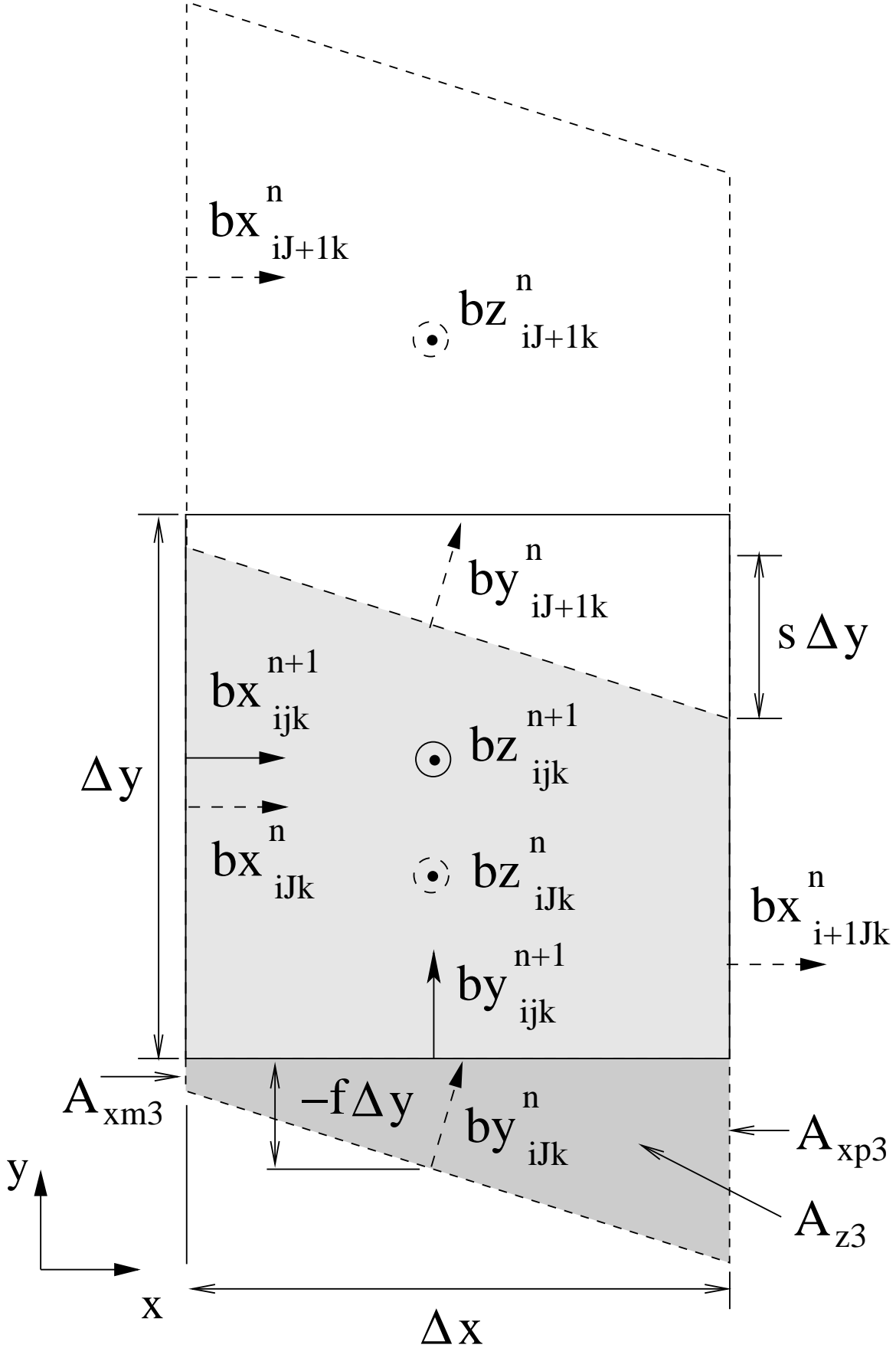
FIG. 4.— A slice in the $x - y$ plane for the Case 3 remap. The dashed lines represent the old grid (n) after it has been distorted by the shear, and the solid square is a new grid zone ($n + 1$) onto which the fluxes are to be mapped. The shaded regions correspond to subvolumes over which the fluxes are summed for the remap of the azimuthal field. See Appendix A for definitions.
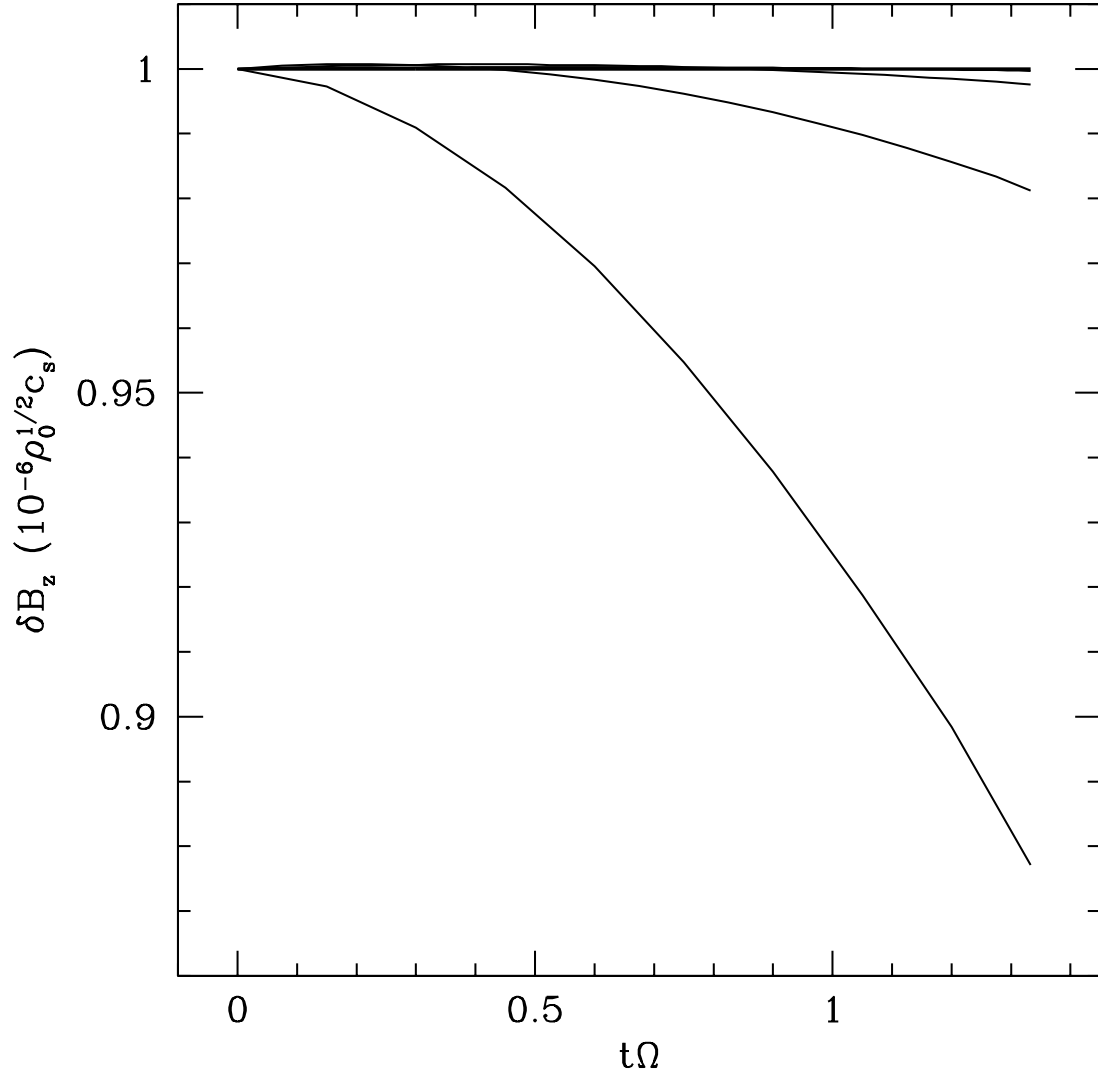
FIG. 5.— Evolution of the vertical field perturbation for a simple advection test. The thick solid line is the expected result, and the thin solid lines correspond to runs at numerical resolutions of $8, 16, 32$ and 64 (from bottom to top). The $N = 64$ curve is indistinguishable from the expected result.
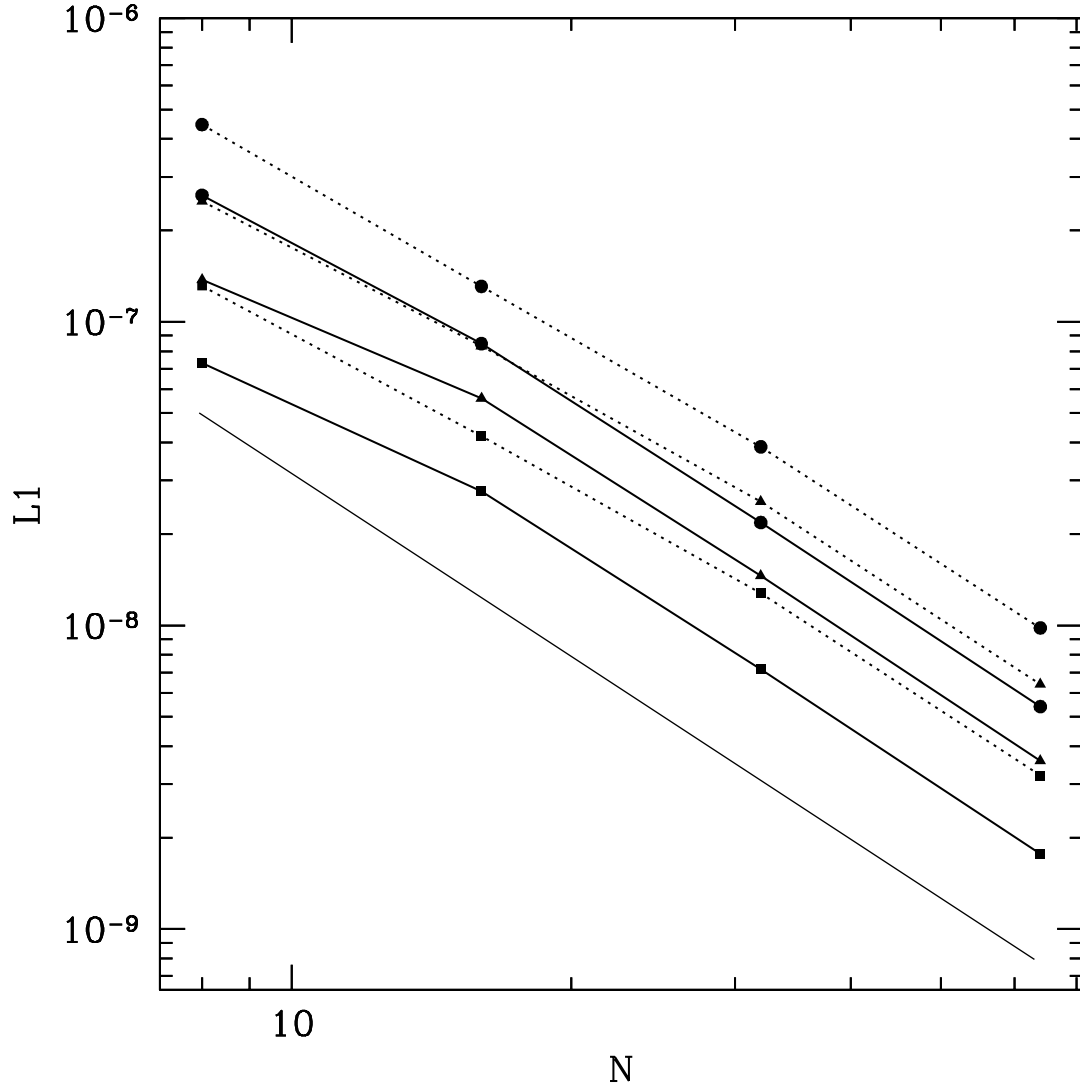
FIG. 6.— Convergence test results with orbital advection on (solid lines) and off (dotted lines). Plotted as a function of numerical resolution N is the L1 norm of the error in each magnetic field component (triangles: B_x, circles: B_y, squares: B_z). The thin solid line is the expected convergence of N^{-2}.
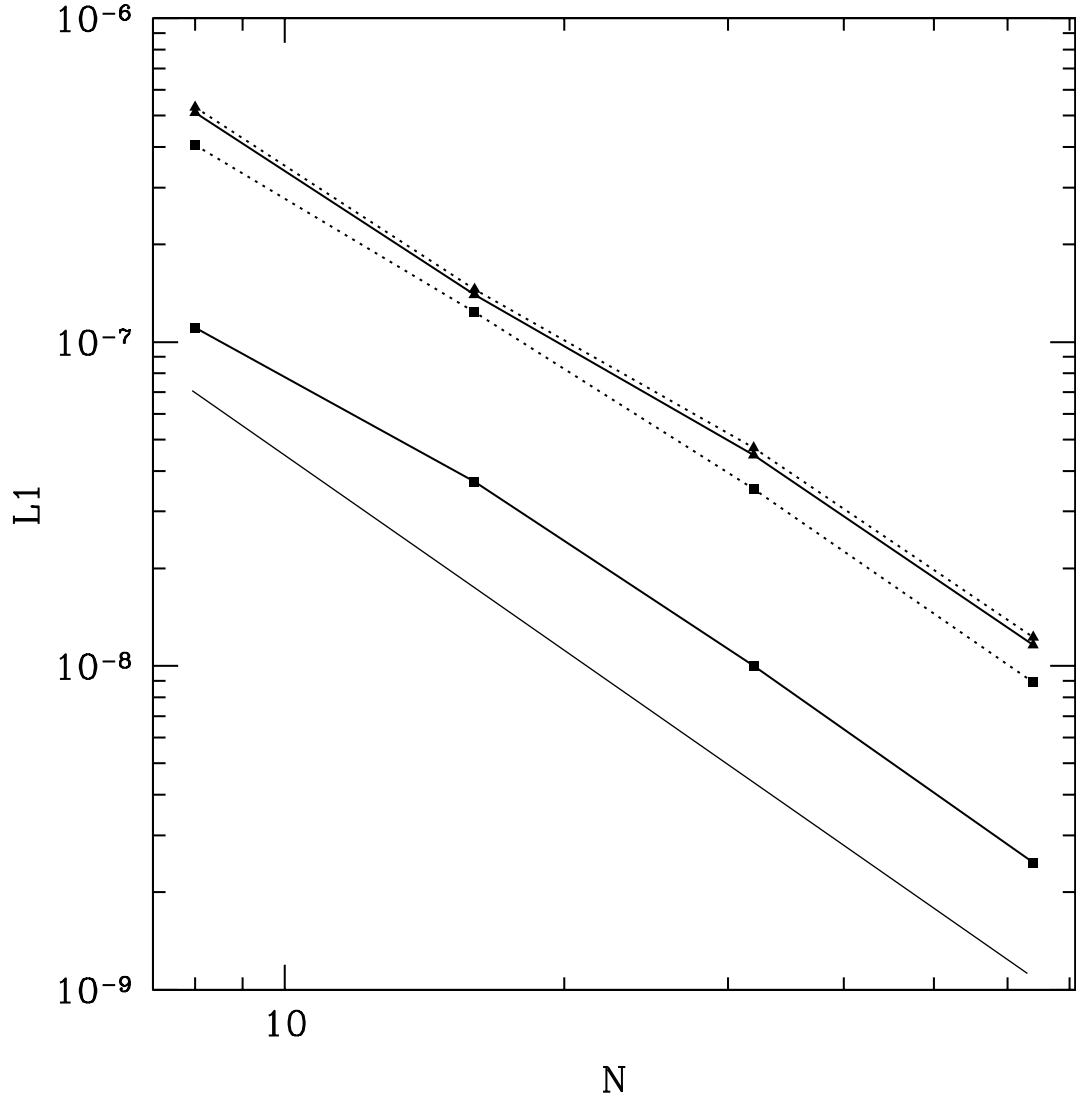
FIG. 7.— Convergence as a function of box size with orbital advection on (solid lines) and off (dotted lines). Plotted as a function of numerical resolution N is the L1 norm of the error in the azimuthal field component with $L = H$ (triangles) and $L = 10H$ (squares). The thin solid line is the expected convergence of N^{-2}.
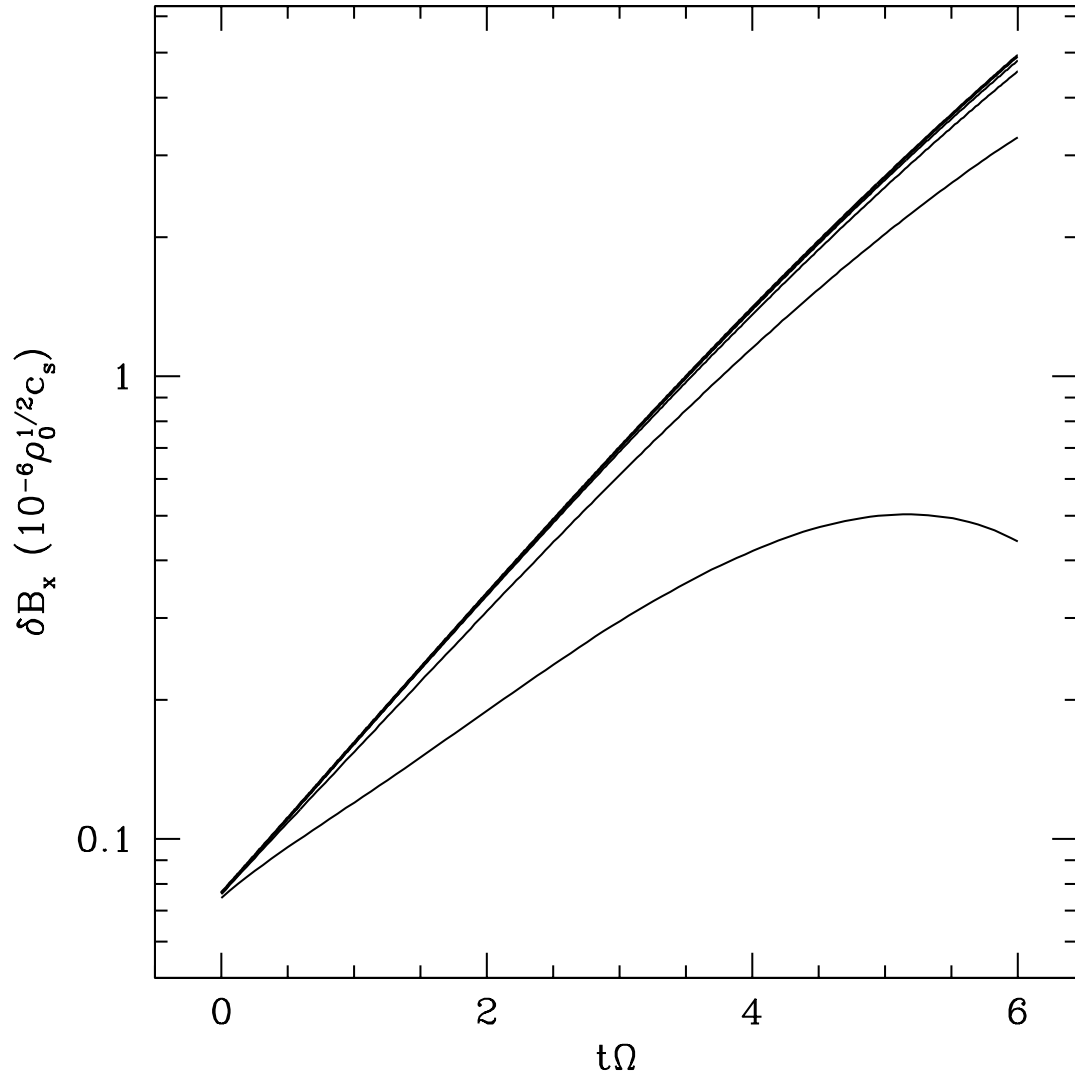
FIG. 8.— Evolution of the radial field perturbation for an incompressive shwave. The thick solid line is the expected result, and the thin solid lines correspond to runs at numerical resolutions of $N_z = 8, 16, 32$ and 64 (from bottom to top). The $N_z = 64$ curve is indistinguishable from the expected result.
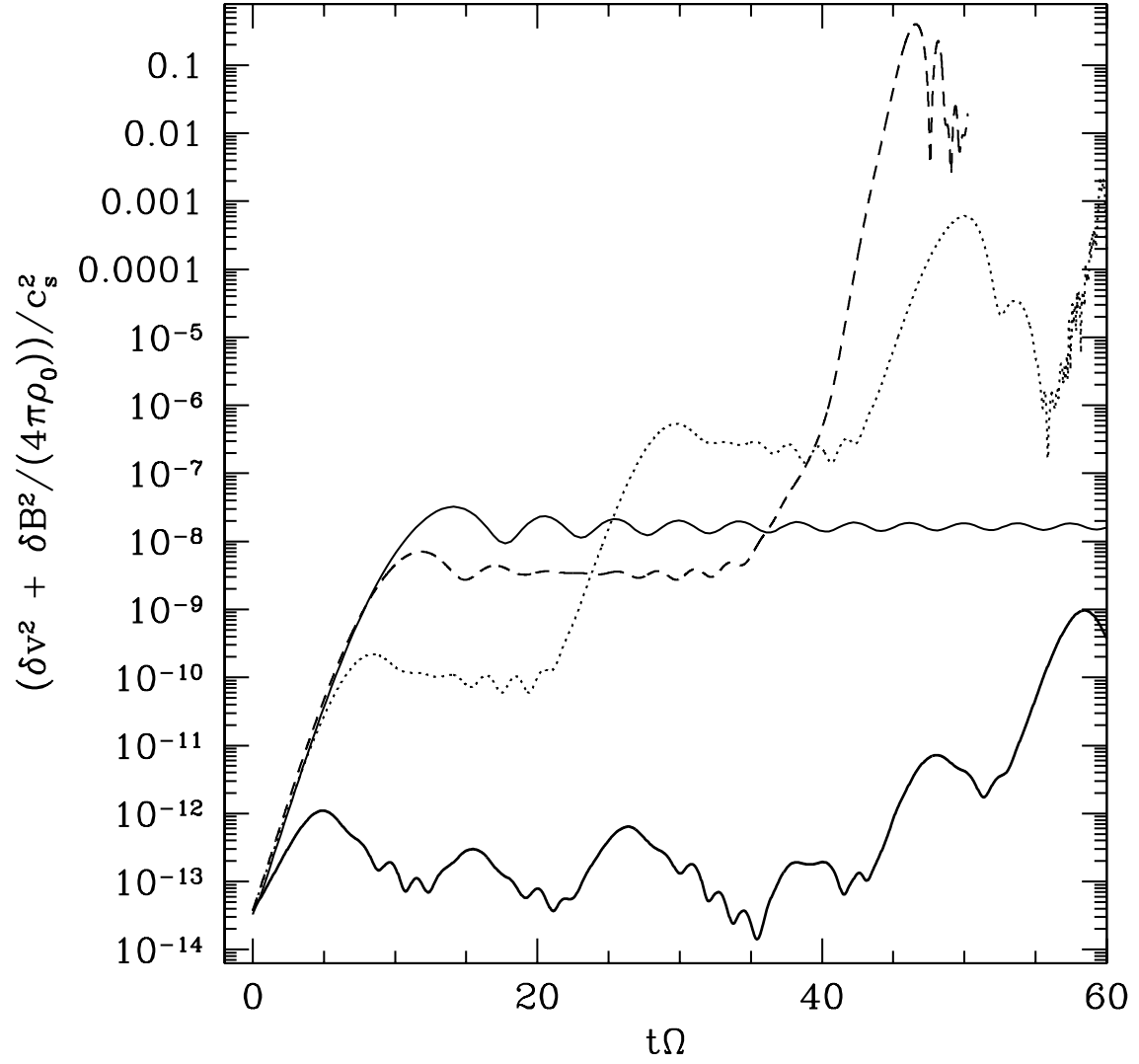
FIG. 9.— The effects of aliasing for the run shown in Figure 8, for numerical resolutions of $N_z = 8$ (heavy solid line), 16 (dotted line) and 32 (dashed line). The light solid curve is the expected result.
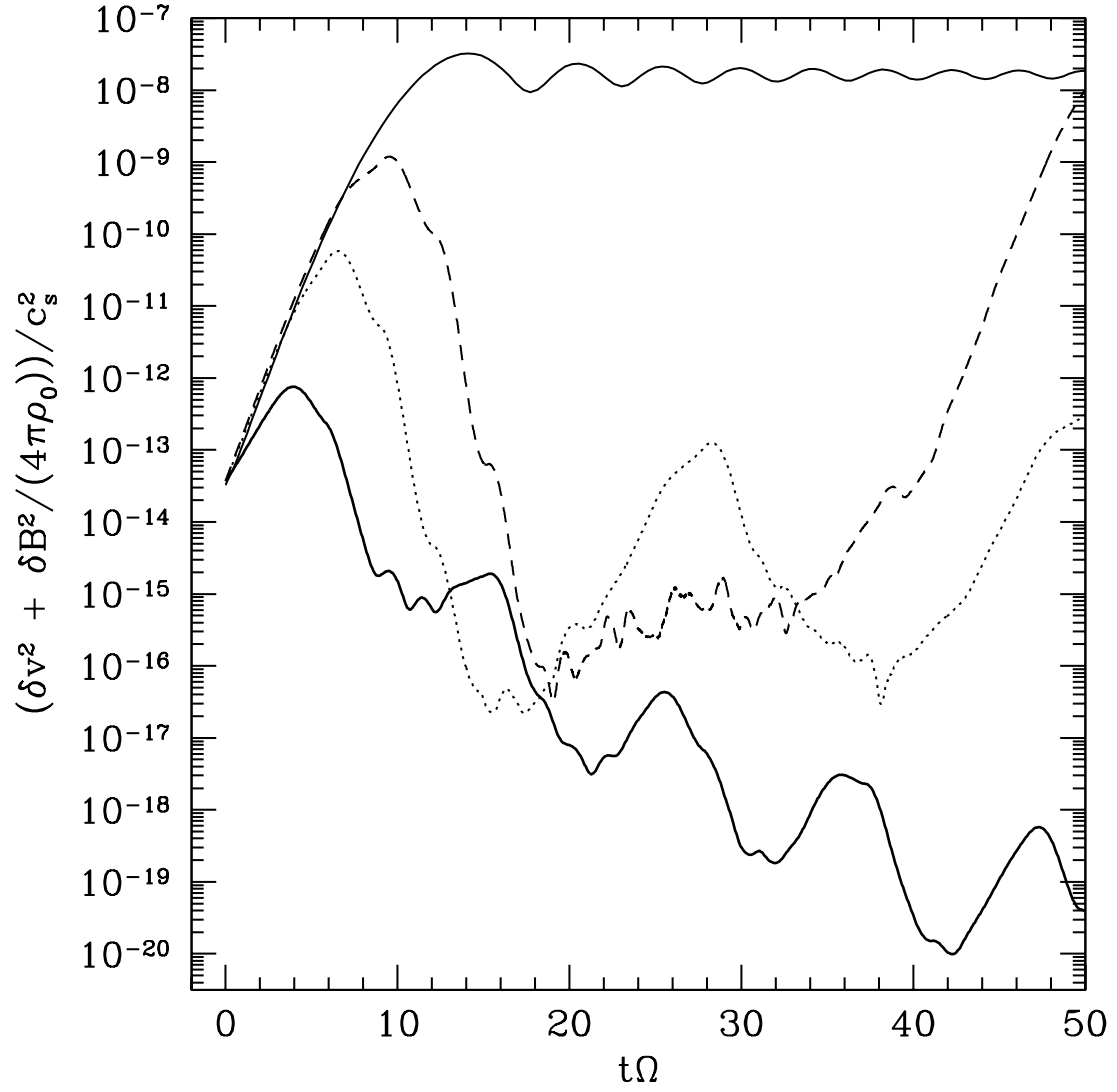
FIG. 10.— Results from the run shown in Figure 9 with an additional bulk epicyclic motion superimposed, for numerical resolutions of $N_z = 8$ (heavy solid line), 16 (dotted line) and 32 (dashed line). The light solid curve is the expected result. See text for discussion.
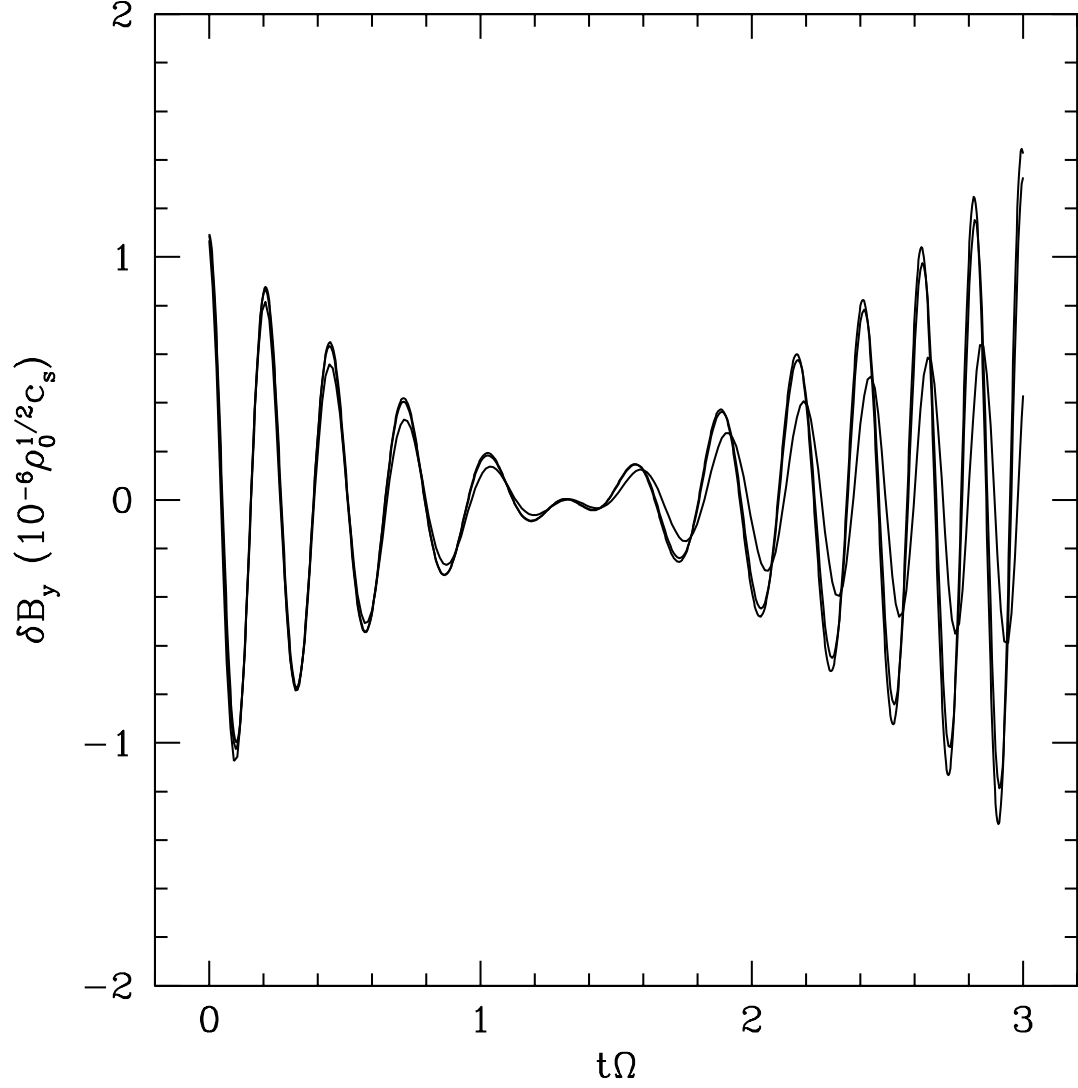
Fig. 11.— Evolution of the azimuthal field perturbation for a compressive shwave. The thick solid line is the expected result, and the thin solid lines correspond to runs at numerical resolutions of $N_z = 8, 16, 32$ and 64. The $N_z = 64$ curve is indistinguishable from the expected result.
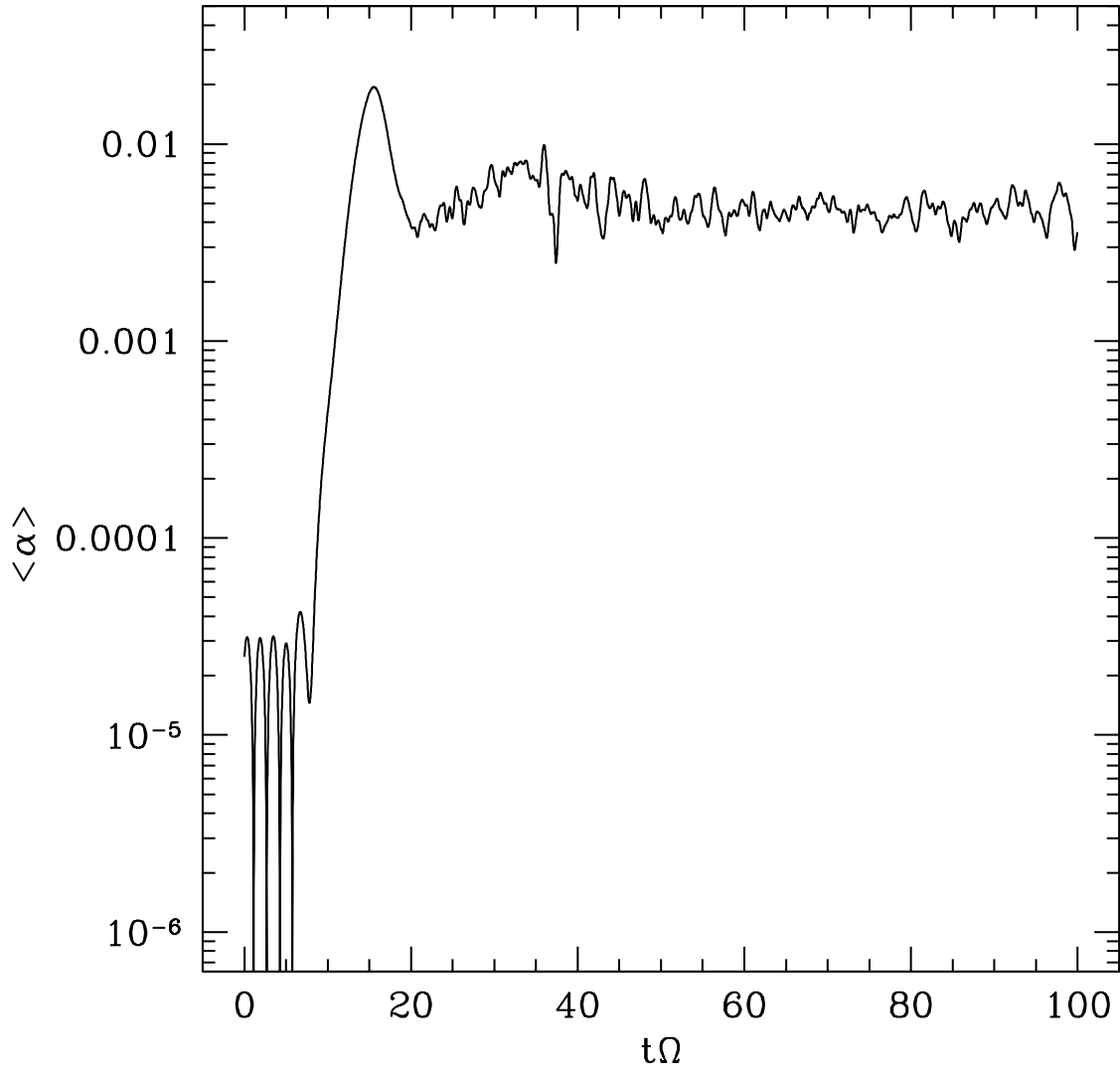
F$_{\text{IG}}$. 12.— Evolution of α in a sample nonlinear calculation. The shearing box model has $L_x \times L_y \times L_z = 8H \times 8\pi H \times 2H$. The "saturated" value of α in this zero-net-field calculation is $\langle \alpha \rangle = 5 \times 10^{-3}$.
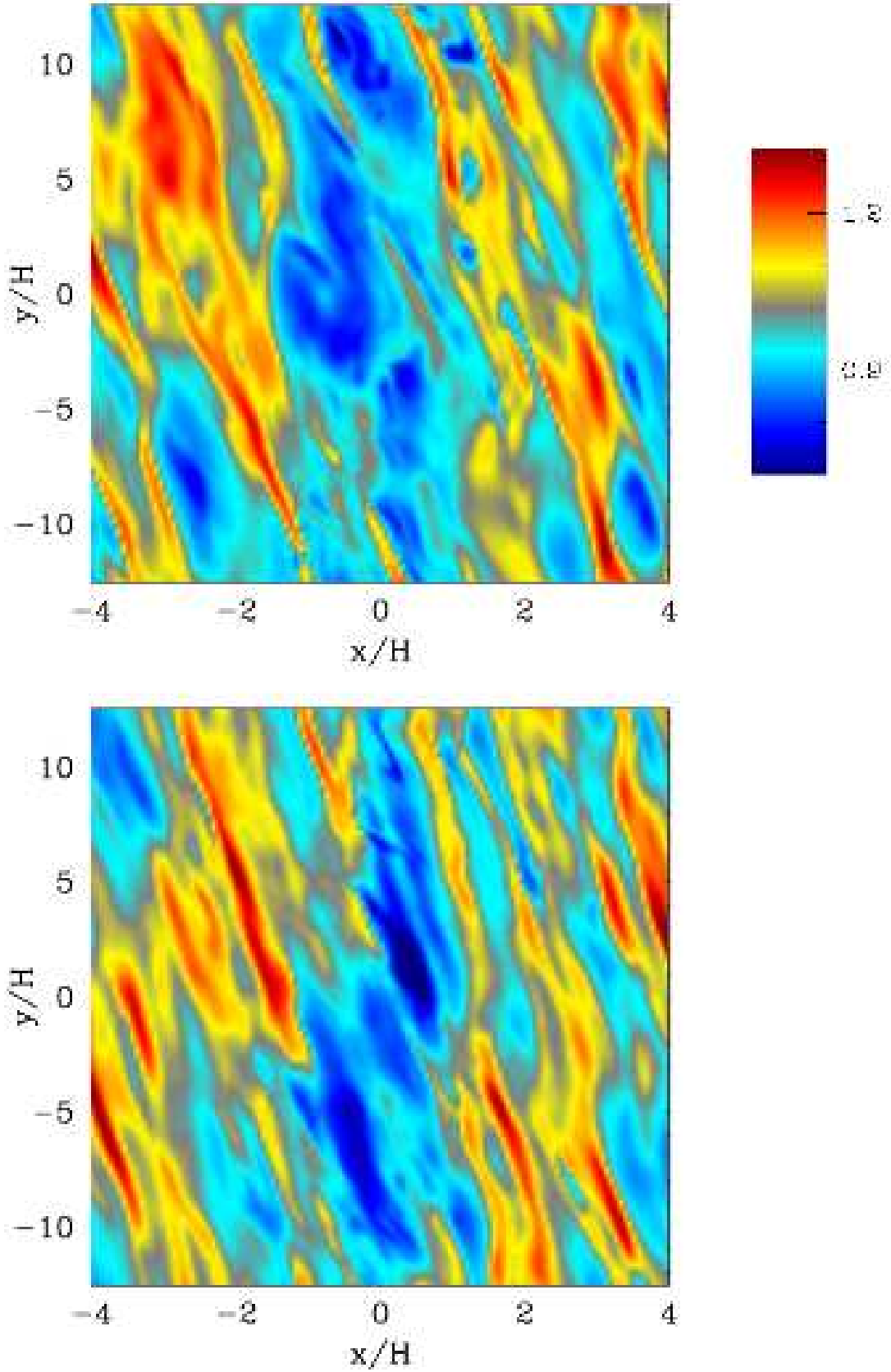
Fig. 13.— Density on a $z = 0$ slice at $t = 100\Omega^{-1}$ in the sample nonlinear calculation with orbital advection (upper panel) and ZEUS (lower panel). A density dip is visible in both images.
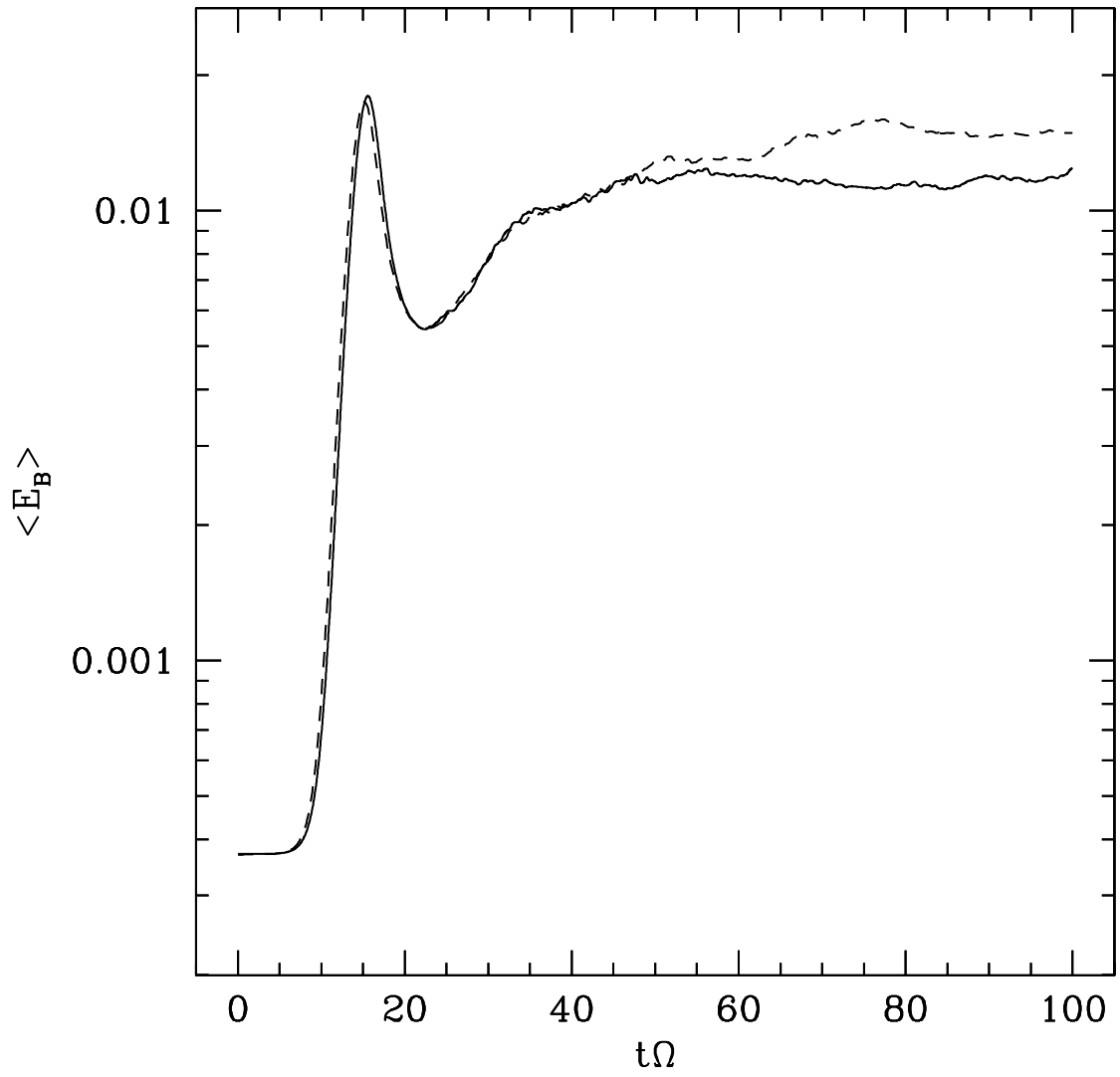
FIG. 14.— Evolution of volume-averaged magnetic energy in the sample nonlinear calculation with orbital advection (solid line) and ZEUS (dashed line).
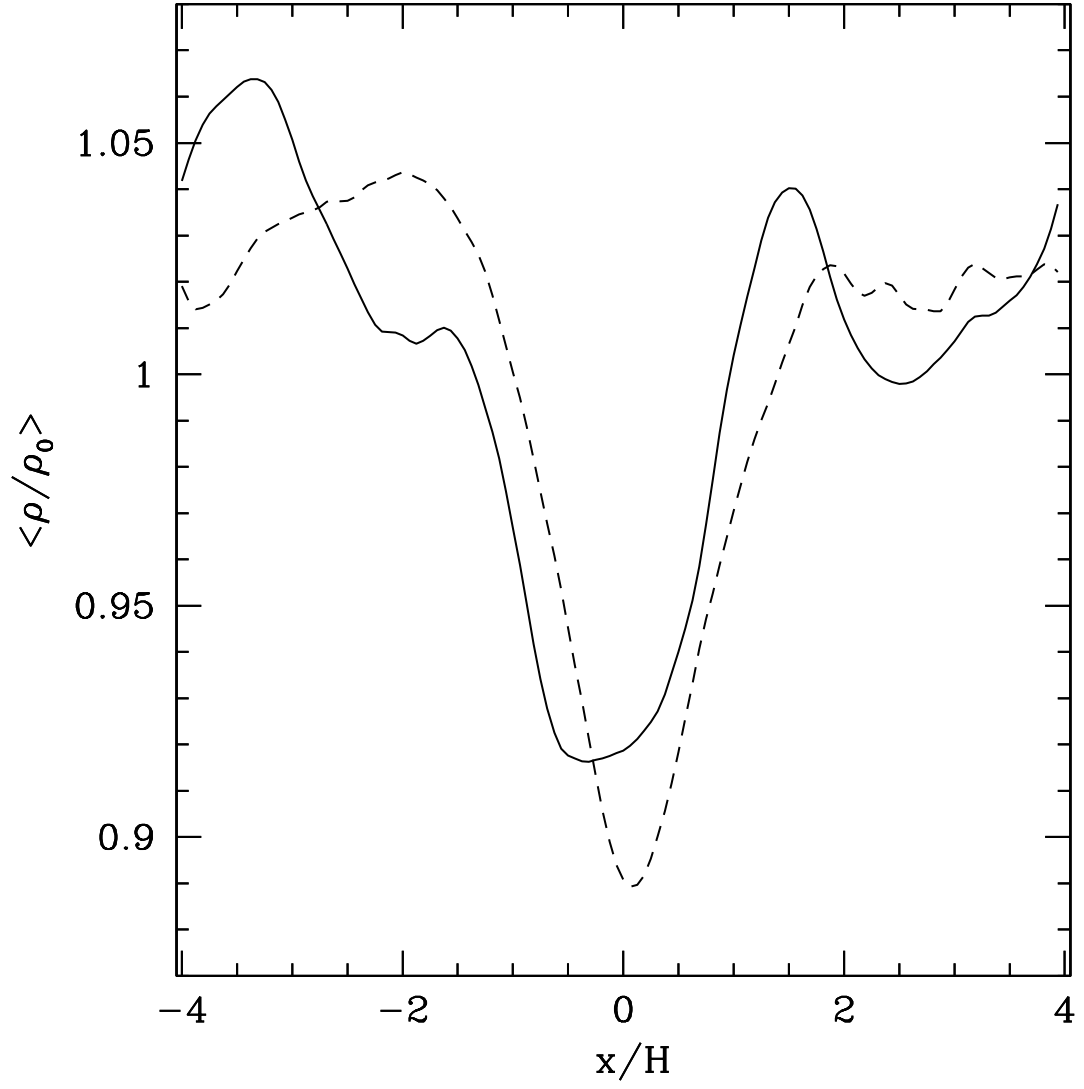
FIG. 15.— Azimuthal and vertical average of the density as a function of x, averaged from $t = 89.5\Omega^{-1}$ to $t = 90.5\Omega^{-1}$ in the sample nonlinear calculation with orbital advection (solid line) and ZEUS (dashed line). Both schemes show a density dip at the center of the box.
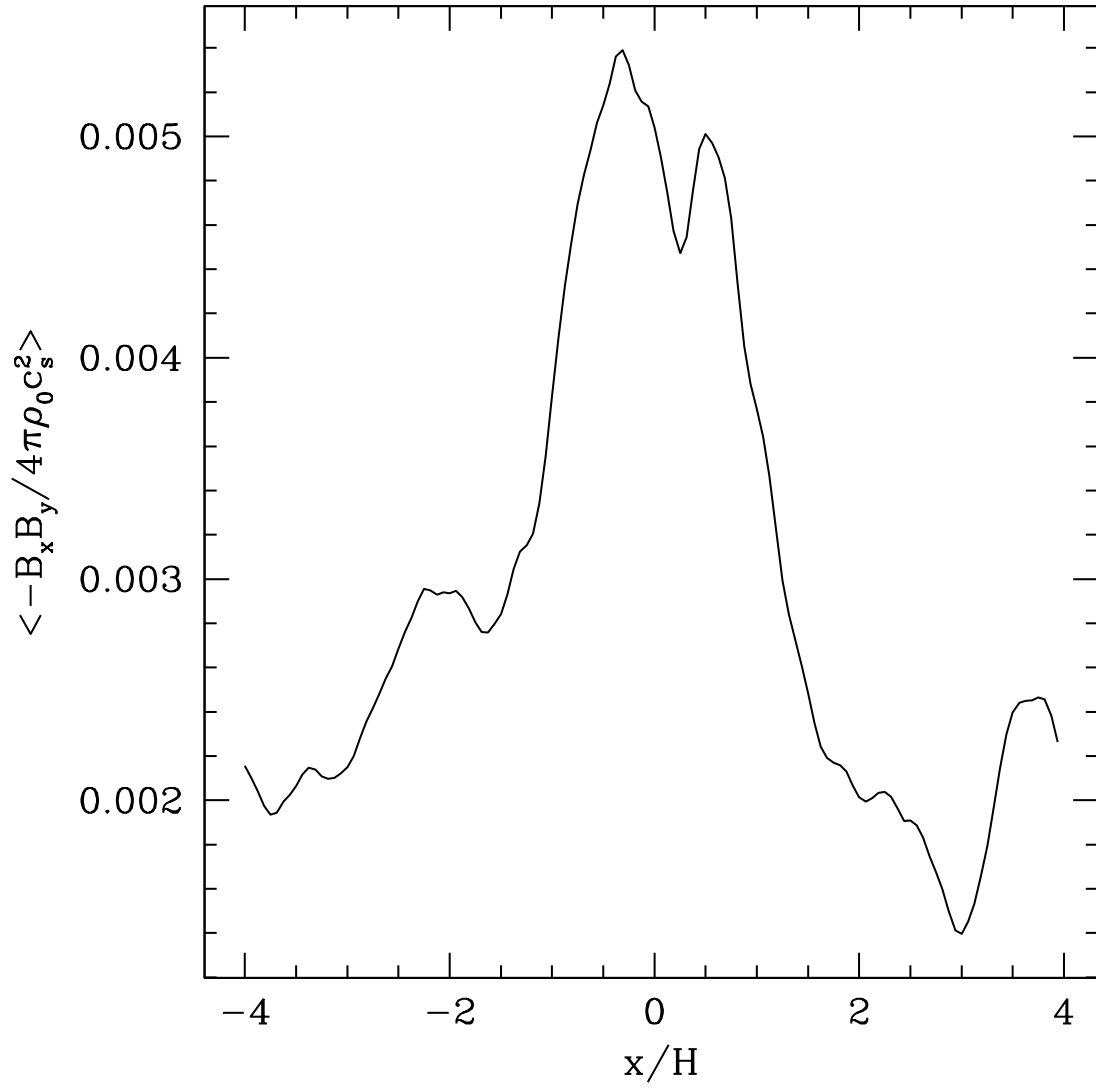
Johnson Guan & Gammie

FIG. 16.— Azimuthal and vertical average of the magnetic stress tensor as a function of x, averaged from $t = 89.5\Omega^{-1}$ to $t = 90.5\Omega^{-1}$ in the sample nonlinear calculation with orbital advection.
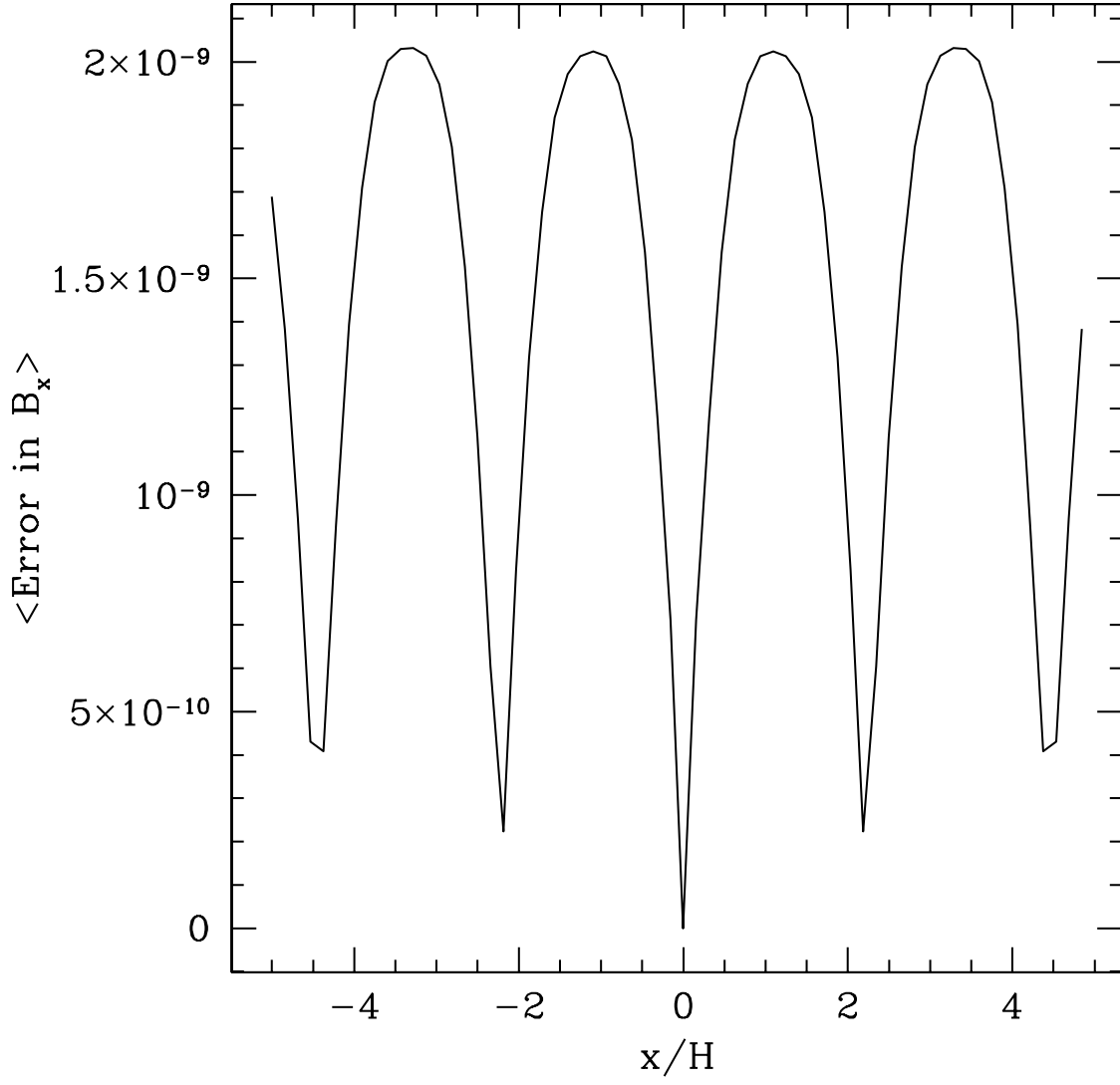
FıG. 17.— Azimuthal and vertical average of the error in B_x as a function of x in a magnetic field advection calculation with orbital advection. The error minima appear at those locations where the cell shift in the orbital advection is an integer.
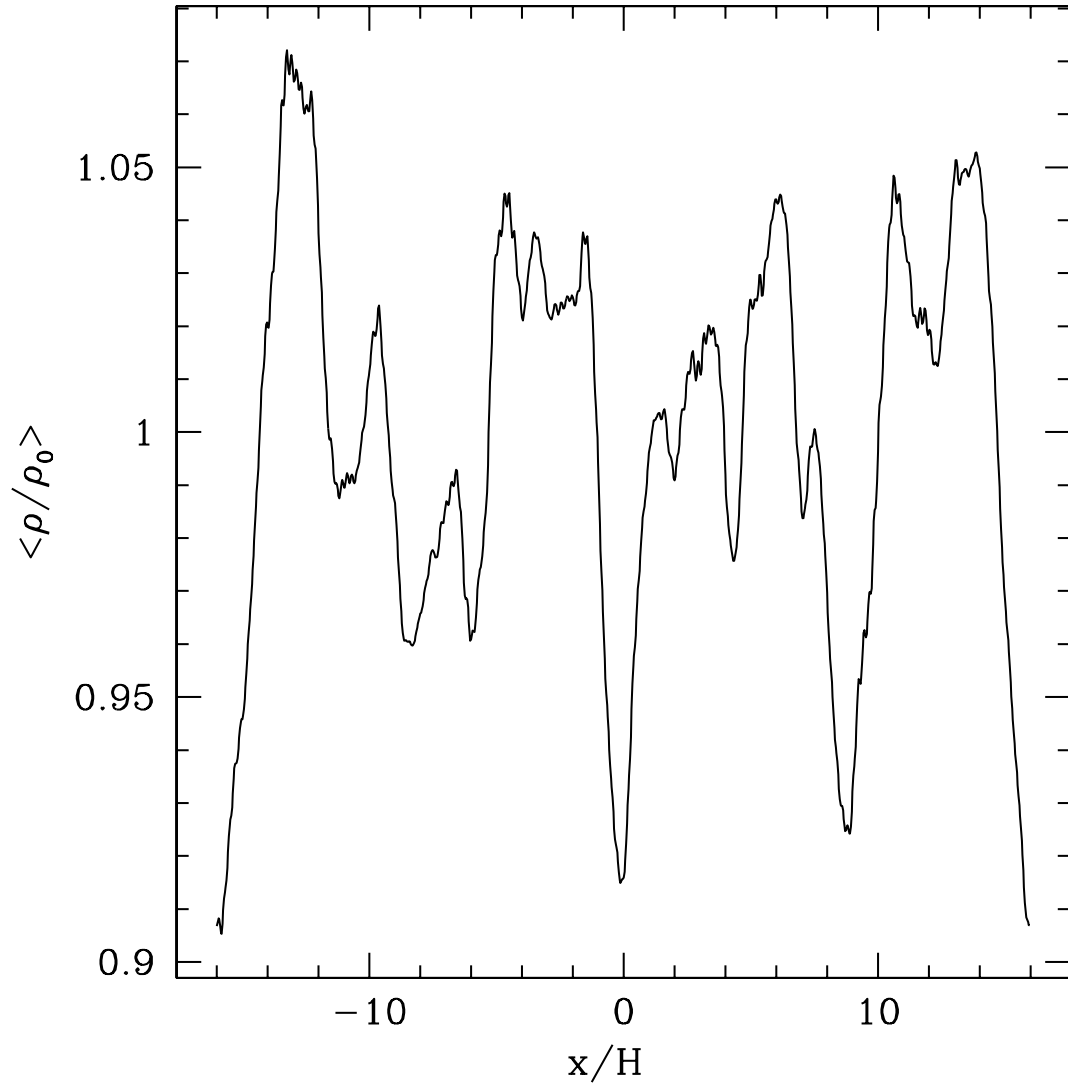
Fig. 18.— Azimuthal and vertical average of the density as a function of x near $t\Omega = 90$ in an $L_x = 32H$ box with orbital advection. The density dips also appear at $x \sim \pm 7H$ where the cell shift is ± 1, and near the edges where the cell shift is ± 2.